

# Bayesian estimation of clustered dependence structures in functional neuroconnectivity

Hyoshin Kim, Sujit Ghosh & Emily C. Hector\*

Department of Statistics, North Carolina State University

## Abstract

Motivated by the need to model joint dependence between regions of interest in functional neuroconnectivity for efficient inference, we propose a new sampling-based Bayesian clustering approach for covariance structures of high-dimensional Gaussian outcomes. The key technique is based on a Dirichlet process that clusters covariance sub-matrices into independent groups of outcomes, thereby naturally inducing sparsity in the whole brain connectivity matrix. A new split-merge algorithm is employed to improve the mixing of the Markov chain sampling that is shown empirically to recover both uniform and Dirichlet partitions with high accuracy. We investigate the empirical performance of the proposed method through extensive simulations. Finally, the proposed approach is used to group regions of interest into functionally independent groups in the Autism Brain Imaging Data Exchange participants with autism spectrum disorder and attention-deficit/hyperactivity disorder.

*Keywords:* Gibbs sampling, Partition learning, Permutation matrix, Slice sampling, Sparse matrix, Stick-breaking construction.

## 1 Introduction

Analyzing functional connectivity in the brain is a crucial task in the study of Autism Spectrum Disorder (ASD). The specific patterns of hyper- and hypoconnectivity between brain regions of interest (ROIs) of autistic versus neurotypical individuals remains poorly understood, with inconsistent findings regarding abnormal functional connectivity in ASD reported in existing neuroimaging studies (Hull et al., 2016). The dominant approach in these studies averages the resting-state fMRI (rfMRI) time series across voxels in each of  $M$  ROIs for each individual  $i \in \{1, \dots, n\}$ . Due to the large number of voxels in each ROI, these averaged rfMRI time series, denoted by  $\{y_{i,t}(r)\}_{r=1}^M$  for time point  $t$  and individual  $i$ , are assumed independently distributed Gaussian owing to the approximation using the Central Limit Theorem. Then, the individual-specific functional connectivity between  $M$  ROIs is estimated by computing the sample correlation between the  $M$  averaged rfMRI time series, treating the time series points as independent replicates. In whole-brain analyses, this connectivity matrix is employed to investigate patterns of coactivation of ROIs across disease status.

---

\*Hector was supported by a grant from the National Science Foundation (DMS2152887) and a Faculty Research and Professional Development Award from North Carolina State University.

The computational complexity associated with the connectivity matrix, which contains  $O(M^2)$  entries for each individual, often leads studies to use coarse parcellations with larger ROIs, such as the Harvard-Oxford atlas with  $M = 111$  or the Craddock 200 atlas with  $M = 200$  (Ha et al., 2015; Ghiassian et al., 2016). Studies aiming to investigate brain functional connectivity at a finer scale typically focus on specific sets of brain regions (Beer et al., 2019; Lynch et al., 2013), thereby limiting the scope of analyses and scientific discoveries. Moreover, multiple analyses focusing on different sets of brain regions run the risk of type-I error inflation, but multiple comparison adjustments are overly conservative when ROIs are correlated. There is thus a need for statistical methodology that estimates functional connectivity between all ROIs in finer brain parcellations while mitigating the computational burden when  $M$  is large.

Motivated by this need, we aim to identify independent groups of correlated ROIs. The independent groups of ROIs identified by our approach can be examined separately in downstream analyses without the fear of loss of statistical power. We propose a sampling based Bayesian clustering approach that partitions the covariance matrix of a high-dimensional Gaussian outcome into structured sub-matrices. We operate in a high-dimensional setting where the number of independent observations, denoted by  $N$ , can be comparable to the number of ROIs. In Section 6, we apply our method to Autism Brain Imaging Data Exchange (ABIDE) data (Di Martino et al., 2014) to identify groups of correlated ROIs in individuals diagnosed with Autism Spectrum Disorder (ASD) and attention-deficit/hyperactivity disorder (ADHD). In this dataset, we use  $M = 1000$  ROIs based on the hierarchical multi-resolution parcellation of Schaefer et al. (2018).

Our underlying assumption is that the outcomes naturally belong to independent groups, leading to a clustering of the covariance sub-matrices. In particular, we assume that the true covariance matrix is a permutation of a block-diagonal matrix composed of structured covariance sub-matrices. This construction ensures that the covariance matrix is positive-definite, capable of accommodating any arbitrary ordering of the ROIs, and flexible in capturing general sparsity patterns.

The modeling of high-dimensional covariance matrices has received considerable attention in the literature. Existing methods that assume a group structure for the outcomes typically assume the group structure to be predetermined or *a priori* known (Li et al., 2015; Luo and Chen, 2020). Examples in spatial settings include spectral methods (Fuentes, 2007), tapered covariance functions (Kaufman et al., 2008; Stein, 2013) and low-rank approximations (Banerjee et al., 2008; Nychka et al., 2015). In contrast, our objective is to learn the group structure through clustering with distinct sets of covariance parameters for each group. Another line of research focused on modeling high-dimensional covariance matrices assumes a general sparsity pattern for the covariance or its inverse, the precision matrix. Bayesian methods in this field employ prior distributions that assign zero probability mass to zero entries while concentrating mass on non-zero entries. Examples include the G-Wishart prior (Roverato, 2002; Mohammadi and Wit, 2015), the Laplace prior (Khondker et al., 2013; Wang, 2012), and the spike-and-slab prior (Samanta et al., 2022; Deshpande et al., 2019). While these methods effectively handle general sparsity patterns, they are more suitable for identifying pairwise relationships between outcomes rather than discovering independent groups of correlated outcomes.

We propose a new Dirichlet process prior for clustering of covariance parameters (Ferguson, 1973). To enhance the mixing of cluster components within a Markov chain based sampling procedure, we present a new Metropolis-Hastings split-merge algorithm called the *Head-Tail Split Merge (HTSM)* algorithm. In various applications, split-merge samplers are employed alongside Gibbs samplers to improve mixing in models using the Dirichlet process, particularly the Dirichlet process mixture model. The state-of-the-art methods in this

domain are the Metropolis-Hastings split-merge samplers proposed by [Dahl \(2003\)](#) and [Jain and Neal \(2004\)](#). Other related approaches include the Metropolis-Hastings Smart-Dumb/Dumb-Smart sampler by [Wang and Russell \(2015\)](#), which combines smart split moves with dumb merge moves or vice versa. The Particle Gibbs Split-Merge sampler introduced by [Bouchard-Côté et al. \(2017\)](#) avoids the need for complex acceptance ratios in Metropolis-Hastings algorithms. Additionally, [Chang and Fisher III \(2013\)](#); [Williamson et al. \(2013\)](#) focus on parallelization and distribution of MCMC methods applicable to split-merge samplers.

Although these existing split-merge samplers are effective, they are primarily designed for clustering in Dirichlet process mixture models. Typically, such models involve a small number of clusters  $J$  and allow for a large dimension  $M$ , resulting in larger-sized clusters due to the nature of mixture models. In contrast, our focus is on clustering covariance sub-matrices, where both  $M$  and  $J$  can be large, allowing for a larger number of smaller-sized clusters, including clusters consisting of a single outcome. To address this scenario, we propose the HTSM algorithm, which can handle these settings effectively.

The HTSM algorithm incorporates two types of proposals: a head split-merge proposal used in conjunction with the slice sampler introduced by [Walker \(2014\)](#), which is aimed at identifying large clusters, and a tail split-merge proposal employed to detect small clusters. In [Section 5](#), we demonstrate empirically that the proposed algorithm can successfully recover both uniform and true Dirichlet partitions when both  $M$  and  $J$  are very large. We also show how to incorporate spatial information to construct the covariance sub-matrices.

The paper is organized as follows. In [Section 2](#), we formulate the Bayesian clustering model for covariance sub-matrices using the stick-breaking representation of the Dirichlet process prior. [Section 3](#) introduces our Slice-within-Gibbs sampler, which is employed to sample the parameters of interest from their corresponding posterior distribution. [Section 4](#) focuses on the sampling of the cluster indices and explores the mixing properties associated with this sampling process. Additionally, this section introduces the HTSM split-merge sampler designed to improve mixing of the proposed clustering approach. The results of simulations are presented in [Section 5](#), and an analysis of the ABIDE data is presented in [Section 6](#). [Section 7](#) concludes.

## 2 Models for clustering covariance sub-matrices

### 2.1 A model for the independent groups of outcomes

Let  $y_i(\mathbf{s}_m)$  be the  $i$ -th observed outcome at location  $\mathbf{s}_m$ ,  $m = 1, \dots, M$ , for the  $m$ -th ROI, and for  $i = 1, \dots, N$  independently. We define  $\mathcal{S}$  as the set of  $M$  locations,  $\mathcal{S} = \{\mathbf{s}_m\}_{m=1}^M$ , with  $\mathbf{s}_m$  the centroid of ROI  $m$ . We define  $\mathbf{y}_i(\mathcal{S}) = \{y_i(\mathbf{s}_1), \dots, y_i(\mathbf{s}_M)\}$ , where the order of the ROIs is arbitrary. Let  $\{\mathbf{X}_i\}_{i=1}^N$  be  $N$   $p$ -dimensional vectors of covariates. We assume that  $\mathbb{E}\{\mathbf{y}_i(\mathcal{S})\} = \mathbf{B}\mathbf{X}_i$  with  $\mathbf{B} = (\boldsymbol{\beta}_1, \dots, \boldsymbol{\beta}_p) \in \mathbb{R}^{M \times p}$  a matrix of regression parameters,  $\boldsymbol{\beta}_q \in \mathbb{R}^M$ ,  $q = 1, \dots, p$ . The variance  $\mathbb{V}\{\mathbf{y}_i(\mathcal{S})\} = \boldsymbol{\Sigma}(\mathcal{S}, \mathcal{S}; \boldsymbol{\theta})$  depends on a vector of covariance parameters  $\boldsymbol{\theta}$  specified below. We assume that the outcomes independently follow  $M$ -variate Gaussian distributions given by

$$\mathbf{y}_i(\mathcal{S}) \sim \mathcal{N}_M\{\mathbf{B}\mathbf{X}_i, \boldsymbol{\Sigma}(\mathcal{S}, \mathcal{S}; \boldsymbol{\theta})\}.$$

We assume that the outcome vector  $\mathbf{y}_i(\mathcal{S})$  can be permuted to construct  $\mathbf{y}_{i,\text{perm}}(\mathcal{S}) = \{y_{i,\text{perm}}(\mathcal{S}_1), \dots, y_{i,\text{perm}}(\mathcal{S}_J)\}$  based on a partition of  $\mathcal{S}$  into  $J$  sets  $\{\mathcal{S}_1, \dots, \mathcal{S}_J\}$ , where outcomes  $y_{i,\text{perm}}(\mathcal{S}_j)$  within a group  $j$  are correlated with each other and outcomes  $y_{i,\text{perm}}(\mathcal{S}_j), y_{i,\text{perm}}(\mathcal{S}_{j'})$  across groups  $j, j'$  are independent.

The independent groups of outcomes induce a block-diagonal structure on  $\mathbb{V}(\mathbf{y}_{i,\text{perm}}\{\mathcal{S}\}) = \boldsymbol{\Sigma}_{\text{perm}}(\mathcal{S}, \mathcal{S}; \boldsymbol{\theta})$ , where the block-diagonal structure is defined as

$$\boldsymbol{\Sigma}_{\text{perm}}(\mathcal{S}, \mathcal{S}; \boldsymbol{\theta}) = \text{Block-diag}\{\boldsymbol{\Sigma}_{\text{perm}}(\mathcal{S}_1, \mathcal{S}_1; \boldsymbol{\theta}_1), \dots, \boldsymbol{\Sigma}_{\text{perm}}(\mathcal{S}_J, \mathcal{S}_J; \boldsymbol{\theta}_J)\}.$$

Each diagonal block covariance is parameterized by a set of variance and correlation parameters  $\boldsymbol{\theta}_j = (\sigma_j^2, \rho_j)$ ,  $j = 1, \dots, J$ , and we denote  $\boldsymbol{\theta} = \{\boldsymbol{\theta}_j\}_{j=1}^J \in \mathbb{R}^{2J}$ . The dimension of each diagonal block is denoted by  $d_j = |\mathcal{S}_j|$ , corresponding to the number of ROIs in the  $j$ -th partition set. We model each diagonal block covariance with

$$\boldsymbol{\Sigma}_{\text{perm}}(\mathcal{S}_j, \mathcal{S}_j; \boldsymbol{\theta}_j) = \sigma_j^2 \boldsymbol{\Gamma}(\mathcal{S}_j, \mathcal{S}_j; \rho_j),$$

where  $\boldsymbol{\Gamma}(\mathcal{S}_j, \mathcal{S}_j; \rho_j)$  is a pre-specified, stationary positive-definite correlation function. This modeling approach allows us to incorporate well-known positive-definite correlation functions, such as compound symmetry, generalized AR(1) (Murray and Helms, 1990), or Matérn (Matérn, 1986) into our modeling framework.

## 2.2 Permutation matrix representation for ordering of outcomes

We introduce the cluster index variable  $Z_m \in \{1, \dots, J\}$  to denote the cluster to which the outcome  $y_i(\mathbf{s}_m)$  belongs. The cluster indices  $\mathbf{Z} = (Z_1, \dots, Z_M)$  induce a partition  $\{\mathcal{S}_1, \dots, \mathcal{S}_J\}$ , where the number of clusters is determined by  $J = \max_m Z_m$ . We define a permutation  $\pi : \{1, \dots, M\} \rightarrow \{1, \dots, M\}$  which rearranges the elements of  $\mathbf{Z}$  in increasing order. The permutation matrix  $\mathbf{P}_\pi$  is constructed by permuting the columns of the identity matrix: the  $m$ -th row of  $\mathbf{P}_\pi$  is a standard basis row vector  $\mathbf{e}_{\pi(m)} \in \mathbb{R}^M$  with zeros in all entries except for a single 1 located in the  $\pi(m)$ -th column. We thus define matrices  $\boldsymbol{\pi}$  and  $\mathbf{P}_\pi$  as

$$\boldsymbol{\pi} = \begin{pmatrix} 1 & 2 & \dots & M \\ \pi(1) & \pi(2) & \dots & \pi(M) \end{pmatrix}; \quad \mathbf{P}_\pi = \begin{pmatrix} \mathbf{e}_{\pi(1)} \\ \mathbf{e}_{\pi(2)} \\ \vdots \\ \mathbf{e}_{\pi(M)} \end{pmatrix}.$$

We illustrate this setup with an example. Consider the outcome vectors  $\mathbf{y}_i(\mathcal{S}) = \{y_i(\mathbf{s}_1), y_i(\mathbf{s}_2), y_i(\mathbf{s}_3), y_i(\mathbf{s}_4), y_i(\mathbf{s}_5)\}$  and  $\mathbf{y}_{i,\text{perm}}(\mathcal{S}) = \{y_i(\mathbf{s}_1), y_i(\mathbf{s}_3), y_i(\mathbf{s}_4) | y_i(\mathbf{s}_2) | y_i(\mathbf{s}_5)\}$ , where the vertical bars indicate the partitioning of the outcomes into independent groups. Here,  $J = 3$ , the cluster indices are  $\mathbf{Z} = (1, 2, 1, 1, 3)$ , and

$$\boldsymbol{\pi} = \begin{pmatrix} 1 & 2 & 3 & 4 & 5 \\ 1 & 3 & 4 & 2 & 5 \end{pmatrix}; \quad \mathbf{P}_\pi = \begin{pmatrix} \mathbf{e}_1 \\ \mathbf{e}_3 \\ \mathbf{e}_4 \\ \mathbf{e}_2 \\ \mathbf{e}_5 \end{pmatrix} = \begin{pmatrix} 1 & 0 & 0 & 0 & 0 \\ 0 & 0 & 1 & 0 & 0 \\ 0 & 0 & 0 & 1 & 0 \\ 0 & 1 & 0 & 0 & 0 \\ 0 & 0 & 0 & 0 & 1 \end{pmatrix}.$$

The permutation matrix systematically recovers  $\boldsymbol{\Sigma}(\mathcal{S}, \mathcal{S}; \boldsymbol{\theta})$  from  $\boldsymbol{\Sigma}_{\text{perm}}(\mathcal{S}, \mathcal{S}; \boldsymbol{\theta})$  through

$$\boldsymbol{\Sigma}(\mathcal{S}, \mathcal{S}; \boldsymbol{\theta}) = \mathbf{P}_\pi^\top \boldsymbol{\Sigma}_{\text{perm}}(\mathcal{S}, \mathcal{S}; \boldsymbol{\theta}) \mathbf{P}_\pi,$$

up to a permutation between blocks, allowing for arbitrary ordering of the diagonal blocks of  $\Sigma_{\text{perm}}$ . It is important to note that this formulation ensures that  $\Sigma$  is essentially equivalent to  $\Sigma_{\text{perm}}$  with its rows and columns permuted. This approach offers several advantages: (i) positive-definiteness of estimators for  $\Sigma$  is guaranteed without requiring additional steps or compromising computational efficiency (ii) arbitrary ordering of the locations is permitted (iii) sparsity observed in the block-diagonal structure of  $\Sigma_{\text{perm}}$  naturally induces sparsity in  $\Sigma$ , enabling flexibility in different sparsity patterns.

### 2.3 Stick-breaking characterization of the Dirichlet process prior

We place a Dirichlet process prior on the distribution of the partition of  $\mathcal{S}$ . Let  $P \sim \text{DP}(\alpha, P_0)$  denote a Dirichlet process prior distribution (Ferguson, 1973) with a scale parameter  $\alpha > 0$  and base distribution  $P_0$ . We adopt the stick-breaking representation of the Dirichlet process prior (Sethuraman, 1994) as follows:

$$\begin{aligned} P &= \sum_{j=1}^{\infty} w_j \delta_{\theta_j} \\ \theta_j &\sim P_0 \text{ for } j \in \mathbb{Z}^+ \\ w_j &= V_j \prod_{l=1}^{j-1} (1 - V_l) \\ V_j &\sim \text{Beta}(1, \alpha) \text{ for } j \in \mathbb{Z}^+, \end{aligned}$$

where  $\delta_{(\cdot)}$  is a measure with a point mass of 1 at  $(\cdot)$ . This representation makes clear that the distribution  $P$  is discrete almost surely. The support of  $P$  consists of a countably infinite set of possible values  $\{\theta_1, \theta_2, \dots\}$  drawn from the base distribution  $P_0$ , and the weights associated with these values are  $\{w_1, w_2, \dots\}$ . The term stick-breaking comes from understanding the construction of  $\{w_1, w_2, \dots\}$  as consecutively breaking a stick of length 1 into an infinite number of pieces. At the  $j$ -th step, the length of the remaining stick is  $\prod_{l=1}^{j-1} (1 - V_l)$ , and a piece of this stick is broken off according to the random variable  $V_j \sim \text{Beta}(1, \alpha)$ . The length of the stick we break off at the  $j$ -th step is assigned to  $w_j$  such that  $\sum_{j=1}^{\infty} w_j = 1$ . The scale parameter  $\alpha$  influences the number of clusters produced by the stick-breaking distribution, with larger  $\alpha$  leading to larger number of clusters on average. We place an additional conjugate prior on  $\alpha$  as  $\alpha \sim \text{Gamma}(a_0, b_0)$  as is commonly used for stick-breaking Dirichlet process priors (Hastie et al., 2015; Ishwaran and James, 2001; Blei and Jordan, 2006).

Under the stick-breaking construction, the prior on the cluster index variable  $Z_m$ ,  $m = 1, \dots, M$ , can be explicitly characterized. The index  $Z_m$  takes value  $j \in \mathbb{Z}^+$  with probability  $w_j$ :

$$\Pr(Z_m = j) = w_j \text{ for } j \in \mathbb{Z}^+, m = 1, \dots, M.$$

The stick-breaking construction naturally leads to an ordering of the cluster labels based on the sizes of the clusters. Specifically,  $\mathbb{E}(w_j) > \mathbb{E}(w_{j+1})$  for all  $j \in \mathbb{Z}^+$  (Papaspiliopoulos and Roberts, 2008). Throughout this paper, we assume that the cluster labels are arranged in decreasing order of cluster size. In this ordering, the largest cluster is assigned the label 1, the second largest cluster is assigned the label 2, and so on.

## 2.4 Priors for regression and covariance parameters

We complete the model formulation by specifying priors for the regression parameters and covariance parameters. We place independent priors on the regression parameters, given by  $\beta_q \sim \mathcal{N}_M(0, \tau^2 \mathbf{I}_M)$ ,  $q = 1, \dots, p$ , where  $\tau$  is a hyperparameter to be specified and  $\mathbf{I}_M \in \mathbb{R}^{M \times M}$  is the identity matrix. It should be noted that there is no assumption of an underlying group structure for the covariates  $\mathbf{X}_i$  or the regression coefficients  $\beta_q$ . This modeling choice is due to the nature of our motivating ABIDE data in Section 6, where the covariates are measured at baseline for each individual and do not vary over  $M$ .

We specify the prior  $\sigma_j^2 \sim \text{Inv-Gamma}(a_1, b_1)$  for the variance parameters  $\sigma_j^2$ ,  $j = 1, 2, \dots$  independently. The range of the correlation parameter  $\rho_j$  depends on the chosen correlation function. We specify the prior distribution for the correlation parameter  $\eta_j \sim \text{Beta}(a_2, b_2)$  where  $\eta_j$  is a suitable transformation of  $\rho_j$  into  $(0, 1)$  based on the correlation function  $\mathbf{\Gamma}(\cdot, \cdot; \rho_j)$ . For example, in the Matérn and generalized AR(1) correlation functions,  $\rho_j$  lies in  $(0, 1)$ , so  $\eta_j = \rho_j$ . In the case of compound symmetry,  $\rho_j$  falls within the range  $(-1/(d_j - 1), 1)$ , and its support depends on  $\mathbf{Z}$ . This poses challenges when updating  $\rho_j$  during the Markov Chain Monte Carlo (MCMC) iterations since the support changes. To address this, we slightly narrow the support to  $\rho_j \in (-1/(M - 1), 1)$ , which ensures positive-definiteness of covariance matrices while maintaining a constant support throughout the iterations. The corresponding transformation is  $\eta_j = (M - 1)\rho_j / M + 1/M$ .

## 3 Slice-within-Gibbs sampler

When sampling from the stick-breaking Dirichlet process prior, it is challenging to directly sample the infinite-dimensional stick-lengths to obtain samples from  $\mathbf{Z}$ . Instead, we use the truncated Dirichlet process introduced by Ishwaran and James (2001). In this approach, we set  $V_K$  to 1, where  $K$  is a fixed value. By doing so, we ensure that for a sufficiently large  $K$ , the infinite sum of stick-lengths,  $\sum_{j=1}^{\infty} w_j = 1$ , can be transformed into a finite sum, such that  $\sum_{j=1}^K w_j = 1$  almost surely. This truncation allows the truncated Dirichlet process to closely approximate the Dirichlet process. We denote the vector of finite-dimensional stick end-points as  $\mathbf{V} = (V_1, \dots, V_K)$ .

The truncation of the stick lengths also leads to the truncation of the number of covariance parameters. Specifically, the number of covariance parameters is truncated at  $K$  and denoted as  $\sigma^2 = (\sigma_1^2, \dots, \sigma_J^2, \sigma_{J+1}^2, \dots, \sigma_K^2)$  and  $\rho = (\rho_1, \dots, \rho_J, \rho_{J+1}, \dots, \rho_K)$ . The value of  $K$  gives the maximum number of clusters allowed in a partition of  $\mathcal{S}$ . By default, we set  $K = M$ . In situations where  $M$  is sufficiently large or when prior knowledge from subject matter science suggests a smaller number of clusters,  $K$  can be reduced, e.g.  $K = M/2$ . Conversely, when  $M$  is small, we set  $K$  to be large, e.g.  $K = 2M$ , to minimize the error

introduced by the truncation. The complete hierarchical model formulation is as follows:

$$\begin{aligned}
\alpha &\sim \text{Gamma}(a_0, b_0) \\
\beta_q &\sim \mathcal{N}_M(0, \tau^2 \mathbf{I}_M) \text{ for } q = 1, \dots, p \\
\theta_j &= (\sigma_j^2, \eta_j) \sim \text{Inv-Gamma}(a_1, b_1) \cdot \text{Beta}(a_2, b_2) \text{ for } j = 1, \dots, K \\
V_j | \alpha &\sim \text{Beta}(1, \alpha) \text{ for } j = 1, \dots, K-1 \text{ and } V_K = 1 \\
w_j &= V_j \prod_{l=1}^{j-1} (1 - V_l) \text{ for } j = 1, \dots, K \\
\mathbf{Z} | \mathbf{V} &\sim \text{Categorical}_K\{w(\mathbf{V})\} \\
\boldsymbol{\Sigma}_{\text{perm}}(\mathcal{S}, \mathcal{S}; \boldsymbol{\theta}) &= \text{Block-diag}\{\boldsymbol{\Sigma}_{\text{perm}}(\mathcal{S}_1, \mathcal{S}_1; \boldsymbol{\theta}_1), \dots, \boldsymbol{\Sigma}_{\text{perm}}(\mathcal{S}_J, \mathcal{S}_J; \boldsymbol{\theta}_J)\} \\
\boldsymbol{\Sigma}(\mathcal{S}, \mathcal{S}; \boldsymbol{\theta}) &= \mathbf{P}_\pi^\top \boldsymbol{\Sigma}_{\text{perm}}(\mathcal{S}, \mathcal{S}; \boldsymbol{\theta}) \mathbf{P}_\pi \\
\mathbf{y}_i(\mathcal{S}) | \mathbf{B}, \mathbf{Z}, \boldsymbol{\theta} &\sim \mathcal{N}_M\{\mathbf{B}\mathbf{X}_i, \boldsymbol{\Sigma}(\mathcal{S}, \mathcal{S}; \boldsymbol{\theta})\} \text{ for } i = 1, \dots, N.
\end{aligned}$$

Given this model formulation, we iteratively sample from the conditional posterior distributions of the variables. This iterative process allows us to obtain values drawn from the complete posterior distribution of  $\{\mathbf{Z}, \mathbf{V}, \boldsymbol{\rho}, \boldsymbol{\sigma}^2, \alpha, \mathbf{B} | \mathbf{Y}(\mathcal{S})\}$  where  $\mathbf{Y}(\mathcal{S}) = \{\mathbf{y}_1(\mathcal{S}), \dots, \mathbf{y}_N(\mathcal{S})\} \in \mathbb{R}^{M \times N}$  is the matrix of outcomes. These samples from the posterior distribution can then be used to infer the distribution of the cluster indices and the covariance matrix.

In section 3.1, we introduce an expression for the likelihood which is used throughout the sampling algorithm. The subsequent sections provide a detailed description of the steps involved in running the Slice-within-Gibbs sampler to draw values from the conditional distributions of  $\mathbf{V}, \boldsymbol{\rho}, \boldsymbol{\sigma}^2, \alpha$ , and  $\mathbf{B}$ . The process of drawing samples for  $\mathbf{Z}$  is outlined separately in Section 4. The sampler iterates between the conditional distributions in the order presented. We denote  $(\cdot)$  as the relevant terms in the posterior with respect to the conditioning parameter. We select only the terms that contain the parameter of interest, discarding all other multiplicative terms as proportionality constants.

### 3.1 Expression for the Likelihood

We present an alternative representation of the likelihood:

$$\begin{aligned}
&p\{\mathbf{Y}(\mathcal{S}) | \mathbf{B}, \mathbf{Z}, \boldsymbol{\rho}, \boldsymbol{\sigma}^2\} \\
&\propto \det\{\boldsymbol{\Sigma}(\mathcal{S}, \mathcal{S}; \boldsymbol{\theta})\}^{-N/2} \exp\left[-\frac{1}{2} \sum_{i=1}^N \{\mathbf{y}_i(\mathcal{S}) - \mathbf{B}\mathbf{X}_i\}^\top \boldsymbol{\Sigma}(\mathcal{S}, \mathcal{S}; \boldsymbol{\theta})^{-1} \{\mathbf{y}_i(\mathcal{S}) - \mathbf{B}\mathbf{X}_i\}\right]. \quad (1)
\end{aligned}$$

The determinant of  $\boldsymbol{\Sigma}(\mathcal{S}, \mathcal{S}; \boldsymbol{\theta})$  in (1) can be expressed as

$$\det\{\boldsymbol{\Sigma}(\mathcal{S}, \mathcal{S}; \boldsymbol{\theta})\} \propto \det\{\boldsymbol{\Sigma}_{\text{perm}}(\mathcal{S}, \mathcal{S}; \boldsymbol{\theta})\} = \prod_{j=1}^J \det\{\boldsymbol{\Sigma}_{\text{perm}}(\mathcal{S}_j, \mathcal{S}_j; \boldsymbol{\theta}_j)\} = \prod_{j=1}^J \sigma_j^{2d_j} \det\{\boldsymbol{\Gamma}(\mathcal{S}_j, \mathcal{S}_j; \rho_j)\}. \quad (2)$$

Here, the terms involving the determinant of  $\mathbf{P}_\pi$  can be treated as constants since the determinant of a permutation matrix is either 1 or  $-1$ . Denoting  $tr(\cdot)$  the trace of a matrix, the terms within the exponential

in equation (1) can be rewritten as

$$\begin{aligned}
& \sum_{i=1}^n \{\mathbf{y}_i(\mathcal{S}) - \mathbf{B}\mathbf{X}_i\}^\top \{\mathbf{P}_\pi^\top \boldsymbol{\Sigma}_{\text{perm}}(\mathcal{S}, \mathcal{S}; \boldsymbol{\theta}) \mathbf{P}_\pi\}^{-1} \{\mathbf{y}_i(\mathcal{S}) - \mathbf{B}\mathbf{X}_i\} \\
&= \sum_{i=1}^n \{\mathbf{y}_i(\mathcal{S}) - \mathbf{B}\mathbf{X}_i\}^\top \mathbf{P}_\pi^\top \boldsymbol{\Sigma}_{\text{perm}}^{-1}(\mathcal{S}, \mathcal{S}; \boldsymbol{\theta}) \mathbf{P}_\pi \{\mathbf{y}_i(\mathcal{S}) - \mathbf{B}\mathbf{X}_i\} \\
&= \text{tr}\{\mathbf{A} \boldsymbol{\Sigma}_{\text{perm}}^{-1}(\mathcal{S}, \mathcal{S}; \boldsymbol{\theta})\} \text{ where } \mathbf{A} = \mathbf{P}_\pi \left[ \sum_{i=1}^n \{\mathbf{y}_i(\mathcal{S}) - \mathbf{B}\mathbf{X}_i\} \{\mathbf{y}_i(\mathcal{S}) - \mathbf{B}\mathbf{X}_i\}^\top \right] \mathbf{P}_\pi^\top \\
&= \sum_{j=1}^J \text{tr}\{\mathbf{A}_j \boldsymbol{\Sigma}_{\text{perm}}^{-1}(\mathcal{S}_j, \mathcal{S}_j; \theta_j)\} \text{ where } \mathbf{A}_j \in \mathbb{R}^{d_j \times d_j} \text{ is the } j^{\text{th}} \text{ diagonal block of } \mathbf{A} \\
&= \sum_{j=1}^J \sigma_j^{-2} \text{tr}\{\mathbf{A}_j \boldsymbol{\Gamma}^{-1}(\mathcal{S}_j, \mathcal{S}_j; \rho_j)\}. \tag{3}
\end{aligned}$$

The first equality follows from the fact that a permutation matrix is an orthogonal matrix. The computational challenges associated with calculating the expensive matrix inverse term  $\boldsymbol{\Sigma}^{-1}$  can be avoided given the block-diagonal structure of  $\boldsymbol{\Sigma}_{\text{perm}}^{-1}$ . By combining terms in equations (2) and (3), the likelihood in equation (1) can be expressed as:

$$p\{\mathbf{Y}(\mathcal{S}) \mid \mathbf{B}, \mathbf{Z}, \boldsymbol{\rho}, \boldsymbol{\sigma}^2\} \propto \left[ \prod_{j=1}^J \sigma_j^{2d_j} \det\{\boldsymbol{\Gamma}(\mathcal{S}_j, \mathcal{S}_j; \rho_j)\} \right]^{-N/2} \exp\left[-\frac{1}{2} \sum_{j=1}^J \sigma_j^{-2} \text{tr}\{\mathbf{A}_j \boldsymbol{\Gamma}^{-1}(\mathcal{S}_j, \mathcal{S}_j; \rho_j)\}\right].$$

### 3.2 Conditional for $\mathbf{V}$

By the conjugacy of the Beta distribution for  $\mathbf{V}$  and the categorical distribution for  $\mathbf{Z}$ , the conditional posterior distribution for  $\mathbf{V}$  is given by

$$p(\mathbf{V} \mid \cdot) \propto p(\mathbf{Z} \mid \mathbf{V}) p(\mathbf{V} \mid \alpha) \propto \prod_{j=1}^K \{w_j(\mathbf{V})^{m_j}\} \prod_{j=1}^{K-1} \{\alpha(1 - V_j)^{\alpha-1}\} \propto \prod_{j=1}^{K-1} \text{Beta}\left(1 + m_j, \alpha + \sum_{\ell=j+1}^K m_\ell\right).$$

Here,  $m_j$  represents the count of instances where  $Z_m = j$  for  $m = 1, \dots, M$ , calculated as  $m_j = \sum_{m=1}^M \mathbb{1}(Z_m = j)$ . To obtain posterior samples of  $V_j$  for  $j = 1, \dots, K - 1$ , we independently draw from the following distribution (recalling  $V_K = 1$ ):

$$p(V_j \mid \cdot) \propto \text{Beta}\left(1 + m_j, \alpha + \sum_{\ell=j+1}^K m_\ell\right).$$

### 3.3 Conditional for $\rho$

The conditional posterior distribution for  $\rho$  can be written as follows:

$$\begin{aligned}
 p(\rho | \cdot) &\propto p\{Y(S) | \mathbf{B}, \mathbf{Z}, \rho, \sigma^2\} p(\rho) \\
 &\propto \prod_{j=1}^J \left[ \det\{\mathbf{\Gamma}(\mathcal{S}_j, \mathcal{S}_j; \rho_j)\}^{-\frac{N}{2}} \exp\left[-\frac{1}{2\sigma_j^2} \text{tr}\{\mathbf{A}_j \mathbf{\Gamma}^{-1}(\mathcal{S}_j, \mathcal{S}_j; \rho_j)\}\right] \eta_j^{a_2-1} (1 - \eta_j)^{b_2-1} \right] \\
 &\quad \prod_{j=J+1}^K \{\eta_j^{a_2-1} (1 - \eta_j)^{b_2-1}\}.
 \end{aligned}$$

At each iteration, for  $j = 1, \dots, J$ , we independently sample  $\rho_j$  with

$$p(\rho_j | \cdot) \propto \det\{\mathbf{\Gamma}(\mathcal{S}_j, \mathcal{S}_j; \rho_j)\}^{-\frac{N}{2}} \exp\left[-\frac{1}{2\sigma_j^2} \text{tr}\{\mathbf{A}_j \mathbf{\Gamma}^{-1}(\mathcal{S}_j, \mathcal{S}_j; \rho_j)\}\right] \eta_j^{a_2-1} (1 - \eta_j)^{b_2-1}.$$

For  $j = J + 1, \dots, K - 1$ , we independently sample  $\rho_j$  from

$$p(\eta_j | \cdot) \propto \text{Beta}(a_2, b_2),$$

where  $\eta_j$  is the variable transformation of  $\rho_j$ . In the case where  $d_j = 1$ , we set  $\rho_j = 0$  because the  $j$ -th sub-matrix has a dimension of one. This sampling procedure can be understood as follows: for  $j = 1, \dots, J$ , where the cluster membership of the  $j$ -th block is updated, we sample  $\rho_j$  by incorporating information from both the likelihood and the prior. However, for  $j = J + 1, \dots, K$ , where the cluster membership of the  $j$ -th block remains unchanged, we update  $\rho_j$  using only the prior information.

We propose to independently sample  $\rho_j$ ,  $j = 1, \dots, J$  in a Gibbs sampling framework using the slice sampler of [Li and Walker \(2020\)](#). A single iteration of Li and Walker's slice sampler to generate a sample for  $\rho_j$  is described in [Algorithm 1](#). Slice sampling is a popular method for generating samples from complex target densities when direct sampling is difficult. Compared to the Metropolis-Hastings algorithm, slice samplers do not require manually specifying the proposal distribution and are known to exhibit good convergence properties. [Roberts and Rosenthal \(1999\)](#) showed that slice samplers have robust geometrically ergodic properties, while [Mira and Tierney \(2002\)](#) established a sufficient condition for uniform ergodicity of slice samplers.

Li and Walker's slice sampler is an extension of Neal's slice sampler ([Neal, 2003](#)), with a modification made to the search component (Step 1 of [Algorithm 1](#)). The advantage of Li and Walker's slice sampler lies in its flexibility and simplicity. Neal's slice sampler uses a while-loop procedure with a fixed step size to search for the value of  $\rho_j$  to sample. In contrast, Li and Walker's slice sampler adds flexibility by introducing a random step size  $s_j$ , eliminating the need for the while-loop component. The variance tuning parameter  $\lambda$  for  $s_j$  can be selected based on prior knowledge about the parameter's support, with Li and Walker recommending a value of either 10 or 100.

---

**Algorithm 1** Li and Walker’s slice sampler (Li and Walker, 2020) for  $\rho_j$

---

**Input:** Current values of  $\rho_0 := \rho_j$ , step-size  $s_0 := s_j$ ; variance tuning parameter  $\lambda$ ; support of  $\rho_j \in (\rho_{\text{lb}}, \rho_{\text{ub}})$

**Output:** Proposed values of  $\rho_j := \rho_1$  and  $s_j := s_1$

1: Sample the slice variable  $\omega \sim U(0, p(\rho_0 | \cdot))$ , and sample

$$l_1 \sim U(\rho_0 - s_0/2, \rho_0 + s_0/2)$$

and  $s_1$  from the density proportional to

$$\exp(-1/\lambda) \mathbb{1}(s_1 > 2|l_1 - \rho_0|)$$

2: If  $\rho_{\text{lb}} < l_1 - s_1/2 < \rho_{\text{ub}}$  then set  $a = l_1 - s_1/2$  else  $a = \rho_{\text{lb}}$

If  $\rho_{\text{lb}} < l_1 + s_1/2 < \rho_{\text{ub}}$  then set  $b = l_1 + s_1/2$  else  $b = \rho_{\text{ub}}$

3: Sample  $\rho^* \sim U(a, b)$ . If  $p(\rho^* | \cdot) > \omega$ , accept  $\rho_1 = \rho^*$ . Else,

$$\text{if } \rho^* < \rho_0 \text{ then } a = \max(a, \rho^*) \text{ else } b = \min(b, \rho^*)$$

4: Repeat Step 3 until  $p(\rho^* | \cdot) > \omega$  and set  $\rho_1 = \rho^*$

---

### 3.4 Conditional for $\sigma^2$

By the conjugacy of the Gaussian likelihood and the Inverse-Gamma prior distribution for  $\sigma^2$ , the conditional posterior distribution for  $\sigma^2$  is given as

$$\begin{aligned} p(\sigma^2 | \cdot) &\propto p\{\mathbf{Y}(\mathcal{S}) | \mathbf{B}, \mathbf{Z}, \boldsymbol{\rho}, \sigma^2\} \\ &\propto \prod_{j=1}^J \text{Inv-Gamma}\left\{a_1 + \frac{Nd_j}{2}, b_1 + \frac{1}{2} \text{tr}(\mathbf{A}_j \boldsymbol{\Gamma}_j^{-1})\right\} \prod_{j=J+1}^K \text{Inv-Gamma}(a_1, b_1). \end{aligned}$$

In a similar manner to sampling the correlation parameters, we independently sample  $\sigma_j^2$  at each iteration for  $j = 1, \dots, J$  from

$$p(\sigma_j^2 | \cdot) \propto \text{Inv-Gamma}\left\{a_1 + \frac{Nd_j}{2}, b_1 + \frac{1}{2} \text{tr}(\mathbf{A}_j \boldsymbol{\Gamma}_j^{-1})\right\}.$$

For  $j = J + 1, \dots, K - 1$ , we independently sample  $\sigma_j^2$  from:

$$p(\sigma_j^2 | \cdot) \propto \text{Inv-Gamma}(a_1, b_1).$$

### 3.5 Conditional for $\alpha$

By the conjugacy of the Beta prior distribution for  $\mathbf{V}$  and the Gamma prior distribution for  $\alpha$ , we sample from the conditional posterior distribution for  $\alpha$ , given by

$$p(\alpha | \cdot) \propto p(\mathbf{V} | \alpha) p(\alpha) \propto \text{Gamma}\left\{a_0 + K - 1, b_0 - \sum_{j=1}^{K-1} \log(1 - V_j)\right\}.$$

### 3.6 Conditional for $\text{vec}(\mathbf{B})$

The form of the conditional posterior distribution for  $\text{vec}(\mathbf{B})$  can be derived as follows. First, we re-express the mean model as:

$$\mathbf{B}\mathbf{X}_i = \left\{ \text{diag}_M(X_{i1}) \quad \text{diag}_M(X_{i2}) \quad \dots \quad \text{diag}_M(X_{ip}) \right\} \begin{pmatrix} \beta_1 \\ \beta_2 \\ \vdots \\ \beta_p \end{pmatrix} = \left( \mathbf{X}_i^\top \otimes \mathbf{I}_M \right) \text{vec}(\mathbf{B}) = \tilde{\mathbf{X}}_i \text{vec}(\mathbf{B})$$

Here,  $\text{diag}_M(X_{iq})$  represents a diagonal matrix of dimension  $M$  with equal diagonal entries  $X_{iq}$ ,  $\tilde{\mathbf{X}}_i = (\mathbf{X}_i^\top \otimes \mathbf{I}_M) \in \mathbb{R}^{M \times Mp}$  and  $\text{vec}(\mathbf{B}) \in \mathbb{R}^{Mp}$ . To simplify notation, we denote  $\boldsymbol{\Sigma} := \boldsymbol{\Sigma}(\mathcal{S}, \mathcal{S}; \boldsymbol{\theta})$  and  $\boldsymbol{\Sigma}_{\text{perm}} := \boldsymbol{\Sigma}_{\text{perm}}(\mathcal{S}, \mathcal{S}; \boldsymbol{\theta})$ . By the conjugacy of the Gaussian likelihood and the Gaussian prior distribution of  $\text{vec}(\mathbf{B})$ , the conditional posterior distribution for  $\text{vec}(\mathbf{B})$  follows the multivariate Gaussian density

$$p\{\text{vec}(\mathbf{B}) | \cdot\} \propto p\{\mathbf{Y}(\mathcal{S}) | \mathbf{B}, \mathbf{Z}, \boldsymbol{\rho}, \boldsymbol{\sigma}^2\} p\{\text{vec}(\mathbf{B})\} \propto \mathcal{N}_{Mp}(\boldsymbol{\mu}, \boldsymbol{\Xi}),$$

where  $\boldsymbol{\Xi}^{-1} := \boldsymbol{\Xi}^{-1}(\mathcal{S}, \mathcal{S}; \boldsymbol{\theta})$  and  $\boldsymbol{\mu} := \boldsymbol{\mu}(\mathcal{S}; \boldsymbol{\theta})$  are defined as

$$\boldsymbol{\Xi}^{-1} = \sum_{i=1}^N \tilde{\mathbf{X}}_i^\top \boldsymbol{\Sigma}^{-1} \tilde{\mathbf{X}}_i + \tau^{-2} \mathbf{I}_{Mp}, \quad \boldsymbol{\mu} = \boldsymbol{\Xi} \sum_{i=1}^N \tilde{\mathbf{X}}_i^\top \boldsymbol{\Sigma}^{-1} \mathbf{y}_i(\mathcal{S}).$$

We further simplify the forms of  $\boldsymbol{\Xi}^{-1}$ ,  $\boldsymbol{\Xi}$  and  $\boldsymbol{\mu}$  to avoid expensive matrix inverse calculations involving  $\boldsymbol{\Sigma}^{-1}$ . We can express  $\boldsymbol{\Xi}^{-1}$  as a product of Kronecker products

$$\begin{aligned} \boldsymbol{\Xi}^{-1} &= (\mathbf{I}_p \otimes \boldsymbol{\Sigma}^{-1}) \left( \sum_{i=1}^N \mathbf{X}_i \mathbf{X}_i^\top \otimes \mathbf{I}_M \right) + \tau^{-2} \mathbf{I}_{Mp} \\ &= (\mathbf{I}_p \otimes \mathbf{P}_\pi^\top) \left( \sum_{i=1}^N \mathbf{X}_i \mathbf{X}_i^\top \otimes \boldsymbol{\Sigma}_{\text{perm}}^{-1} + \tau^{-2} \mathbf{I}_{Mp} \right) (\mathbf{I}_p \otimes \mathbf{P}_\pi), \end{aligned}$$

where the first equality follows from noting that  $\tilde{\mathbf{X}}_i$  is a block matrix composed of row binding  $\text{diag}_M(X_{iq})$ ,  $q = 1, \dots, p$ . The eigendecomposition of the  $p \times p$  real symmetric matrix  $\sum_{i=1}^N \mathbf{X}_i \mathbf{X}_i^\top$  and the  $M \times M$  real symmetric matrix  $\boldsymbol{\Sigma}_{\text{perm}}^{-1}$  yields  $\sum_{i=1}^N \mathbf{X}_i \mathbf{X}_i^\top = \mathbf{Q}_1 \boldsymbol{\Lambda}_1 \mathbf{Q}_1^\top$  and  $\boldsymbol{\Sigma}_{\text{perm}}^{-1} = \mathbf{Q}_2 \boldsymbol{\Lambda}_2 \mathbf{Q}_2^\top$ , respectively. Here,  $\boldsymbol{\Lambda}_1$  and  $\boldsymbol{\Lambda}_2$  are diagonal matrices, and  $\mathbf{Q}_1$  and  $\mathbf{Q}_2$  are orthogonal matrices. Substituting these expressions into  $\boldsymbol{\Xi}$  yields

$$\boldsymbol{\Xi} = \left\{ (\mathbf{Q}_1 \otimes \mathbf{P}_\pi^\top \mathbf{Q}_2) (\boldsymbol{\Lambda}_1 \otimes \boldsymbol{\Lambda}_2 + \tau^{-2} \mathbf{I}_{Mp})^{-1/2} \right\} \left\{ (\mathbf{Q}_1 \otimes \mathbf{P}_\pi^\top \mathbf{Q}_2) (\boldsymbol{\Lambda}_1 \otimes \boldsymbol{\Lambda}_2 + \tau^{-2} \mathbf{I}_{Mp})^{-1/2} \right\}^\top := \mathbf{U} \mathbf{U}^\top. \quad (4)$$

This reduces the computationally intensive inverse of a  $Mp \times Mp$  matrix to a computation of the inverse square root of the diagonal matrix  $\mathbf{U}$ . Since  $\boldsymbol{\Sigma}_{\text{perm}}^{-1}$  is a block diagonal matrix, we can reduce computational time by separately performing the eigendecomposition of each main diagonal block to obtain  $\mathbf{Q}_2$  and  $\boldsymbol{\Lambda}_2$ . The eigendecomposition for  $\sum_{i=1}^N \mathbf{X}_i \mathbf{X}_i^\top$  is performed once at the beginning of the sampling algorithm. Similarly,

we express  $\boldsymbol{\mu}$  as follows:

$$\boldsymbol{\mu} = \Xi \text{vec} \left\{ \mathbf{P}_\pi^\top \boldsymbol{\Sigma}_{\text{perm}}^{-1} \mathbf{P}_\pi \sum_{i=1}^N \mathbf{y}_i(\mathcal{S}) \mathbf{X}_i^\top \right\}. \quad (5)$$

By combining the terms in equations (4) and (5), we sample  $\text{vec}(\mathbf{B})$  from the following distribution:

$$\text{vec}(\mathbf{B}) = \boldsymbol{\mu} + \mathbf{U}\boldsymbol{\nu}, \quad \boldsymbol{\nu} \sim \mathcal{N}_{Mp}(\mathbf{0}, \mathbf{I}_{Mp}).$$

## 4 Split-merge sampler for cluster indices $\mathbf{Z}$

Sampling the cluster indices  $\mathbf{Z}$  can be a challenging task as the number of possible partitions of a set, the Bell number, is excessively large. Even for small values of  $M$ , such as  $M = 10$ , the Bell number exceeds  $10^5$ . The challenge becomes more significant when the number of clusters  $J$  is high, and a large number of parameters  $\boldsymbol{\theta}_j$ ,  $j = 1, \dots, J$ , need to be estimated. The intrinsic difficulty in exploring the partition space efficiently causes many MCMC samplers for models that use the Dirichlet process prior to suffer from poor mixing issues. [Hastie et al. \(2015\)](#) note that samplers developed for the Dirichlet process mixture model are typically illustrated on low dimensional data sets, where the values of  $M$  and/or  $J$ , are small, and the poor mixing issues that arise for moderate to high dimensional data sets are not fully explored. This section first demonstrates that similar mixing issues occur for our clustering algorithm. We then propose a hybrid sampler that combines the slice sampler of [Walker \(2014\)](#) with a new split-merge algorithm called the Head-Tail Split-Merge (HTSM) sampler presented in Section 4.2. To investigate the efficiency of our proposed sampler, we conduct simulations in Section 5 on data sets with very large values of  $M$  and  $J$ . Our results show that the proposed sampler performs well, even for high-dimensional data sets with a large number of clusters.

### 4.1 Poor mixing of Gibbs type samplers for $\mathbf{Z}$

Let  $\mathbf{Z}_{-m}$  represent the sub-vector of  $\mathbf{Z}$  obtained by removing the  $m$ -th coordinate. We consider sampling each  $Z_m$  for  $m \in \{1, \dots, M\}$  according to its full conditional posterior distribution, conditional on all other variables, as

$$p(Z_m = j \mid \mathbf{Z}_{-m}, \cdot) \propto p\{\mathbf{Y}(\mathcal{S}) \mid \mathbf{B}, (Z_1, \dots, Z_{m-1}, j, Z_{m+1}, \dots, Z_M), \boldsymbol{\theta}\} \\ \cdot p\{(Z_1, \dots, Z_{m-1}, j, Z_{m+1}, \dots, Z_M) \mid \mathbf{V}\},$$

for  $j = 1, \dots, K$ . In the Gibbs sampler,  $Z_m$  is drawn from the distribution with point mass probabilities

$$\left( \frac{p_1}{\sum_{j=1}^K p_j} \quad \cdots \quad \frac{p_K}{\sum_{j=1}^K p_j} \right)$$

at values  $\{1, \dots, K\}$ . Here,  $p_j := p(Z_m = j \mid \mathbf{Z}_{-m}, \cdot)$ , and  $p_j / \sum_{j=1}^K p_j$  represents the probability that the  $m$ -th outcome belongs to the  $j$ -th cluster. The Gibbs sampler searches over the indices  $\{1, \dots, K\}$  for each outcome, resulting in computationally intensive  $O(MK)$  operations at each MCMC iteration. Walker’s slice sampler is a discrete adaptation of Li and Walker’s slice sampler ([Li and Walker, 2020](#)) that is applicable to discrete sample spaces. The sampling steps for  $Z_m$  in Walker’s slice sampler are presented in Algorithm 2. The key distinction between Walker’s slice sampler and Li and Walker’s slice sampler lies in the treatment of

the step-size  $s \in \mathbb{Z}^+$ . In Walker’s slice sampler, the step-size is fixed and chosen to be a large value to ensure effective exploration of the discrete sample space. At each MCMC iteration, Walker’s slice sampler searches over the cluster indices  $\{1, \dots, \min(Z_m + s - 1, K)\}$  for each outcome, which requires fewer operations on average compared to the  $O(MK)$  complexity of the Gibbs sampler. By default, we set  $s = K/2$ .

---

**Algorithm 2** Walker’s slice sampler (Walker, 2014) for  $Z_m$

---

**Input:** Current values of  $\mathbf{Z}$  and  $z_0 := Z_m$ ; support of  $Z_m \in \{1, \dots, K\}$ ; step-size  $s \in \mathbb{R}^+$

**Output:** Proposed value of  $Z_m := z_1$

1: Sample the slice variable  $\omega \sim U(0, p(Z_m = z_0 | \mathbf{Z}_{-m}, \cdot))$ , and sample

$$l_1 \sim U\{z_0, \min(z_0 + s - 1, K)\}$$

2: Set  $a = 1$  and  $b = l_1$

3: Sample  $Z^* \sim U\{a, b\}$ . If  $p(Z_m = z^* | \mathbf{Z}_{-m}, \cdot) > \omega$ , accept  $z_1 = z^*$ . Else,

$$\text{if } z^* < z_0 \text{ then } a = \max(a, z^*) \text{ else } b = \min(b, z^*)$$

4: Repeat Step 3 until  $p(Z_m = z^* | \mathbf{Z}_{-m}, \cdot) > \omega$  and set  $z_1 = z^*$

---

Figure 1 provides an illustrative example that highlights the poor mixing behavior of the commonly used Gibbs sampler and Walker’s slice sampler (Walker, 2014). It depicts the maximum a posteriori (MAP) estimates of the conditional posterior distribution of  $\mathbf{Z}$  obtained using the Gibbs sampler and Walker’s slice sampler. The true partition is generated either from a  $\text{DP}(4, P_0)$  distribution ( $J = 14$ ) or from a uniform distribution with equal partition sizes ( $J = 20$ ). The data dimensions are  $M = 100$  and  $N = 100$ , with a generalized AR(1) covariance structure in each cluster. Both the Gibbs sampler and Walker’s slice sampler have difficulty escaping the local mode of the partition space, resulting in MAP estimates that fail to accurately identify the true partition.

In this example, however, Walker’s slice sampler exhibits better performance in terms of proximity to the true partition. It requires fewer split-merge steps to recover the true partition compared to the Gibbs sampler. Split steps involve selecting a cluster and dividing its elements into two clusters, while merge steps involve selecting two clusters and merging them into a single cluster. The split-merge steps required for the MAP estimates to reach the true partition are highlighted by grey and blue bars for split and merge steps, respectively in Figure 1. An interesting observation from Figure 1 is that i) a larger number of split steps are typically needed to recover the true partition compared to merge steps, and ii) split steps tend to occur more frequently in clusters of larger and smaller sizes, termed the head and tail of the partition respectively. Specifically, Gibbs-type samplers often result in larger clusters being grouped together and becoming larger than the true partition, while also encountering difficulties in splitting smaller clusters into clusters of size one.

This motivates the development of a new sampling algorithm that improves mixing of  $\mathbf{Z}$  by performing additional split-merge steps to Walker’s slice sampler. The Metropolis-Hastings rejection-sampling approach for split-merge steps has been used with standard Gibbs steps to address the issue of slow convergence and poor mixing of the Gibbs sampler (Green and Richardson, 2001; Dahl, 2003; Jain and Neal, 2004; Wang and Russell, 2015) for models using the Dirichlet process prior, particularly in the context of Dirichlet process mixture models. Although these existing split-merge samplers have proven effective, they are primarily

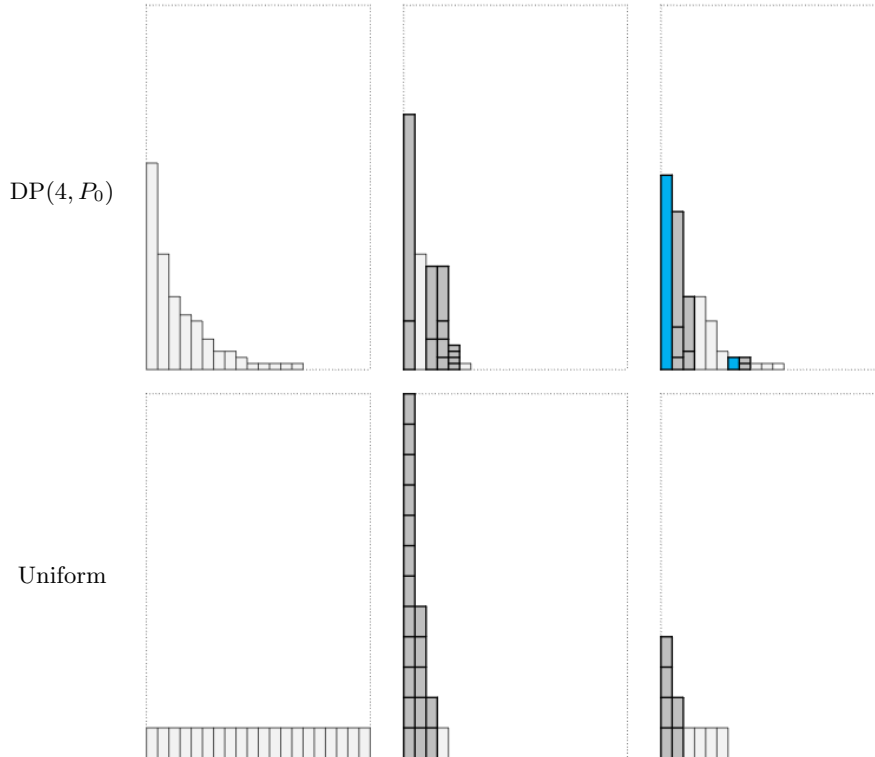


Figure 1: The true partition (left) and MAP estimate of the partition obtained from the Gibbs sampler (middle) and Walker’s slice sampler (right). The true partition is generated from a  $DP(4, P_0)$  (top) or a uniform distribution with equal partition sizes (bottom), with  $M = 100$  and  $N = 100$ , assuming a generalized AR(1) covariance structure in each cluster. The cluster labels are sorted by size from largest to smallest. Highlighted grey bars indicate additional split steps needed to reach the true partition; highlighted blue bars indicate additional merge steps needed to reach the true partition. The MAP estimate of the partition obtained from our proposed clustering method recovers the true partition.

tailored for clustering in Dirichlet process mixture models that typically involve a small number of clusters where  $M$  and/or  $J$  are small. In contrast, our focus is on clustering covariance sub-matrices where both  $M$  and  $J$  are large, enabling a greater number of smaller-sized clusters, including single-outcome clusters. To address this specific scenario, we propose the Head-Tail Split-Merge (HTSM) sampler, which effectively handles these settings.

## 4.2 Head-Tail Split-Merge (HTSM) sampler

Two state-of-the-art algorithms for split-merge samplers are described in [Jain and Neal \(2004\)](#) and [Dahl \(2003\)](#). In [Jain and Neal \(2004\)](#), two indices are selected at random from  $\{1, \dots, M\}$ . If the two indices do not belong to the same cluster, a merge move is proposed. Otherwise, if the two indices are in the same  $j$ -th cluster, a split move is proposed, with one index assigned to the  $j$ -th cluster and the other assigned to a new  $(J + 1)$ -th cluster, and all other indices that were in the  $j$ -th cluster are randomly assigned to one of these two clusters. Restricted Gibbs steps are applied several times inside the two clusters to reassign the indices to one of the two clusters, while all other clusters remain unchanged. The modified  $\mathbf{Z}$  after the

intermediate restricted Gibbs steps, termed as the *launch state*, is used to generate the final split after one last restricted Gibbs step. The Metropolis-Hastings acceptance ratio is calculated to accept or reject the split or merge move.

Dahl (2003) proposed an alternative split procedure that avoids the complicated intermediate restricted Gibbs steps of Jain and Neal (2004). One index is assigned to the  $j$ -th cluster, the other index is assigned to a new  $(J + 1)$ -th cluster. All other indices remaining in the  $j$ -th cluster are randomly permuted, then sequentially assigned to one of the two clusters using the restricted Gibbs sampler, conditioned on the previously allocated indices.

Our proposed HTSM sampler offers two types of split-merge moves: head or tail. We define the head of the partition as the larger clusters, and the tail as the smaller clusters. A head split-merge is a split or merge move applied to the head of a partition, and a tail split-merge is a split or merge move applied to the tail of a partition. The HTSM sampler consists of two phases: the first phase typically corresponds to the first half of the MCMC, and the second phase typically corresponds to the second half:

- In the first phase, the HTSM sampler alternates between Walker’s slice sampler and a head split-merge that proposes a head split or merge with probabilities of  $p_0$  and  $1 - p_0$ , respectively.
- In the second phase, the HTSM sampler proposes a tail split or merge with probabilities of  $p_0$  and  $1 - p_0$ , respectively. This move can detect small clusters that require splitting into clusters of size one.

To ensure that the cluster labels are arranged correctly from largest to the smallest, relabeling is performed after the HTSM sampler during each iteration of the MCMC.

Our approach of using  $p_0$  to decide between a split or merge move allows us to control the proportion of split and merge moves. We set the default value of  $p_0$  to 0.7 to encourage split moves to occur more frequently than merge moves. Note that our approach of using  $p_0$  differs from the approaches in Jain and Neal (2004) and Dahl (2003), where a pair of indices are uniformly chosen to determine a split or merge move based on whether the selected pair is in the same cluster or not. Wang and Russell (2015) used a similar approach to ours by pre-selecting the split-merge move type, but they chose their split-merge moves uniformly.

The split step across the first and second phase is characterized by two different vectors that encourage splitting in the large versus small clusters, respectively. On the other hand, merge steps across both phases give equal probability to all clusters, regardless of their size, to be merged. Below, we describe the probability vectors that favor large and small clusters, as well as the implementation details for the split-merge moves. Let  $\mathbf{Z}^*$  and  $\boldsymbol{\theta}^*$  be the candidate states which we will consider for the split-merge proposal. Denote  $J^+$  as the number of clusters of size greater than one. The proposed HTSM sampler is outlined in Algorithm 3.

If a merge proposal, where  $(\mathbf{Z}^*, \boldsymbol{\theta}^*) = (\mathbf{Z}^{\text{merge}}, \boldsymbol{\theta}^{\text{merge}})$ , is being considered, the sampler selects two clusters, the  $j$ -th and the  $j'$ -th cluster uniformly at random from the set of  $J$  clusters. The indices  $\{Z_m^* : Z_m^* = j\}$  and  $\{Z_m^* : Z_m^* = j'\}$  within both clusters are then assigned to the  $j$ -th cluster, with the covariance parameter  $\boldsymbol{\theta}_{j'}^*$  updated by setting it equal to  $\boldsymbol{\theta}_j^*$ .

In the case of a head split proposal, where  $(\mathbf{Z}^*, \boldsymbol{\theta}^*) = (\mathbf{Z}^{\text{split}}, \boldsymbol{\theta}^{\text{split}})$ , we construct a decreasing probability vector  $\mathbf{p}_{\text{split}} \in \mathbb{R}^{J^+}$ . By sampling a cluster to split randomly using  $\mathbf{p}_{\text{split}}$ , a preference is given to selecting larger clusters for the split move. In the simulations and data analysis, for a head split proposal, we choose  $\mathbf{p}_{\text{split}}$  to be proportional to the Dirichlet process stick-breaking lengths  $\{w_1, \dots, w_{J^+}\}$  constructed by setting  $V_j = 0.3$  for all  $j = 1, \dots, J^+$ . This ensures that for large enough  $J^+$ , the probability of selecting the largest cluster for splitting is approximately 0.3, the probability of selecting the second largest cluster is approximately

0.2, the probability of selecting the third largest cluster is approximately 0.15, and the probability of selecting the fourth largest cluster is approximately 0.1. Approximately 75% of the split moves will occur within the four largest clusters.

On the other hand, if a tail split proposal is chosen, an increasing probability vector  $\mathbf{p}_{\text{split}} \in \mathbb{R}^{J^+}$  is constructed, and a cluster to split is randomly chosen based on this vector, resulting in a tendency to choose smaller clusters. In the simulations and data analysis, for the tail split proposal, we choose  $\mathbf{p}_{\text{split}}$  as the reverse of that for the head split proposal.

After selecting the  $j$ -th cluster for splitting, we first prepare the launch state by randomly assigning the indices  $\{Z_m^*\} = \{Z_m^* : Z_m^* = j\}$  within that cluster to either the same  $j$ -th cluster or a new  $(J+1)$ -th cluster. Additionally, the covariance parameter  $\theta_{J+1}^*$  is updated by assigning it the value of  $\theta_j^*$ . Then, the indices  $\{Z_m^*\}$  are sequentially assigned to one of the two clusters according to the conditional posterior distributions  $p(Z_m^* = j | \mathbf{Z}_{-m}^*, \boldsymbol{\theta}^*, \cdot)$  and  $p(Z_m^* = J+1 | \mathbf{Z}_{-m}^*, \boldsymbol{\theta}^*, \cdot)$  using the restricted Gibbs sampler.

---

**Algorithm 3** Head-Tail Split-Merge sampler

---

**Input:** Current values of  $\mathbf{Z}, \boldsymbol{\theta}$ ; split-merge probability  $p_0$ ; Head-Tail type,  $type_{\text{HT}} \in \{\text{H}, \text{T}\}$

**Output:** Proposed values of  $\mathbf{Z}, \boldsymbol{\theta}$

- 1: Choose the split-merge move type with probability

$$\Pr(type = \text{split}) = p_0 \text{ and } \Pr(type = \text{merge}) = 1 - p_0.$$

- 2: Set candidate states as  $\mathbf{Z}^*$  and  $\boldsymbol{\theta}^*$ .

- 3: If  $type_{\text{HT}} == \text{H}$ , then  $\mathbf{p}_{\text{split}} \in \mathbb{R}^{J^+}$  is a decreasing probability vector.

Else if  $type_{\text{HT}} == \text{T}$ , then  $\mathbf{p}_{\text{split}} \in \mathbb{R}^{J^+}$  is an increasing probability vector.

- 4: If  $type == \text{split}$ :

Choose the  $j$ -th cluster to split according  $\mathbf{p}_{\text{split}}$ .

Prepare the launch state by randomly assigning indices  $\{Z_m^*\} = \{Z_m^* : Z_m^* = j\}$  into one of the two clusters:  $j$  or  $(J+1)$ .

Set  $\theta_{J+1}^* := \theta_j^*$ .

Assign  $\{Z_m^*\}$  sequentially into the  $j$  or  $(J+1)$ -th cluster according to probabilities

$$p(Z_m^* = j | \mathbf{Z}_{-m}^*, \boldsymbol{\theta}^*, \cdot) \text{ and } p(Z_m^* = J+1 | \mathbf{Z}_{-m}^*, \boldsymbol{\theta}^*, \cdot).$$

- 5: Else if  $type == \text{merge}$ :

Choose the  $j$  and  $j'$ -th clusters to merge uniformly from the  $J$  clusters.

Assign the indices  $\{Z_m^* : Z_m^* = j\}$  and  $\{Z_m^* : Z_m^* = j'\}$  to the  $j$ -th cluster.

Set  $\theta_{j'}^* := \theta_j^*$ .

- 6: Calculate the Metropolis-Hastings acceptance probability

$$\alpha^* = \min \left[ 1, \frac{q\{(\mathbf{Z}, \boldsymbol{\theta}) | (\mathbf{Z}^*, \boldsymbol{\theta}^*), \cdot\} p\{\mathbf{Y}(\mathcal{S}) | \mathbf{Z}^*, \boldsymbol{\theta}^*, \cdot\} p(\mathbf{Z}^* | \mathbf{V}) p(\boldsymbol{\theta}^*)}{q\{(\mathbf{Z}^*, \boldsymbol{\theta}^*) | (\mathbf{Z}, \boldsymbol{\theta}), \cdot\} p\{\mathbf{Y}(\mathcal{S}) | \mathbf{Z}, \boldsymbol{\theta}, \cdot\} p(\mathbf{Z} | \mathbf{V}) p(\boldsymbol{\theta})} \right],$$

and accept the proposal with probability  $\alpha^*$ .

---

It remains to calculate the Metropolis-Hastings acceptance probability for the HTSM sampler, which

takes the form

$$\alpha^* = \min \left[ 1, \frac{q\{(\mathbf{Z}, \boldsymbol{\theta}) | (\mathbf{Z}^*, \boldsymbol{\theta}^*), \cdot\} p\{\mathbf{Y}(\mathcal{S}) | \mathbf{Z}^*, \boldsymbol{\theta}^*, \cdot\} p(\mathbf{Z}^* | \mathbf{V}) p(\boldsymbol{\theta}^*)}{q\{(\mathbf{Z}^*, \boldsymbol{\theta}^*) | (\mathbf{Z}, \boldsymbol{\theta}), \cdot\} p\{\mathbf{Y}(\mathcal{S}) | \mathbf{Z}, \boldsymbol{\theta}, \cdot\} p(\mathbf{Z} | \mathbf{V}) p(\boldsymbol{\theta})} \right], \quad (6)$$

where  $(\mathbf{Z}^*, \boldsymbol{\theta}^*)$  is either  $(\mathbf{Z}^{\text{split}}, \boldsymbol{\theta}^{\text{split}})$  or  $(\mathbf{Z}^{\text{merge}}, \boldsymbol{\theta}^{\text{merge}})$  depending on the type of proposal, and  $q\{(\mathbf{Z}, \boldsymbol{\theta}) | (\mathbf{Z}^*, \boldsymbol{\theta}^*), \cdot\}$  and  $q\{(\mathbf{Z}^*, \boldsymbol{\theta}^*) | (\mathbf{Z}, \boldsymbol{\theta}), \cdot\}$  are transition probabilities from  $(\mathbf{Z}^*, \boldsymbol{\theta}^*)$  to  $(\mathbf{Z}, \boldsymbol{\theta})$  and from  $(\mathbf{Z}, \boldsymbol{\theta})$  to  $(\mathbf{Z}^*, \boldsymbol{\theta}^*)$  respectively. Here, we factored the posterior distribution into a product of the likelihood and the prior, and ignored terms not involving  $(\mathbf{Z}, \boldsymbol{\theta})$  or  $(\mathbf{Z}^*, \boldsymbol{\theta}^*)$ .

A graphical presentation of the transition probabilities for HTSM split-merge proposals is shown as a directed acyclic graph (DAG) in Figure 2. We can calculate the individual terms in Equation (6) as follows.

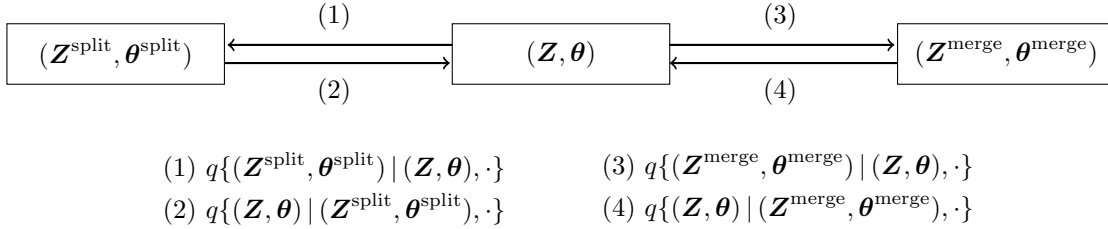


Figure 2: The DAG presenting the transition probabilities for a split-merge proposal of the HTSM.

- The split proposal probability  $q\{(\mathbf{Z}^{\text{split}}, \boldsymbol{\theta}^{\text{split}}) | (\mathbf{Z}, \boldsymbol{\theta}), \cdot\}$  can be expressed as

$$\begin{aligned} q\{(\mathbf{Z}^{\text{split}}, \boldsymbol{\theta}^{\text{split}}) | (\mathbf{Z}, \boldsymbol{\theta}), \cdot\} &= q\{\mathbf{Z}^{\text{split}} | \boldsymbol{\theta}^{\text{split}}, (\mathbf{Z}, \boldsymbol{\theta}), \cdot\} q\{\boldsymbol{\theta}^{\text{split}} | (\mathbf{Z}, \boldsymbol{\theta}), \cdot\} \\ &= q(\mathbf{Z}^{\text{split}} | \boldsymbol{\theta}^{\text{split}}, \mathbf{Z}, \cdot) \\ &= \left(\frac{1}{2}\right)^{d_j} \prod_{m \in \mathcal{I}_{d_j}} p(Z_m = z_m^{\text{split}} | \mathbf{Z}_{-m}, \boldsymbol{\theta}^{\text{split}}, \cdot), \end{aligned}$$

where  $\mathcal{I}_{d_j}$  denotes the set of coordinates for the  $j$ -th cluster. The second equality is derived by observing that splitting the cluster indices vector is only influenced by  $(\mathbf{Z}, \boldsymbol{\theta}^{\text{split}})$ , and not by  $\boldsymbol{\theta}$ . Additionally,  $q\{\boldsymbol{\theta}^{\text{split}} | (\mathbf{Z}, \boldsymbol{\theta}), \cdot\} = 1$  since there is only one way to split the covariance parameter given  $(\mathbf{Z}, \boldsymbol{\theta})$ . The last equality is the multiplication of two terms: the first term represents the probability of proposing a split move from the original state to the launch state  $(1/2^{d_j})$ . The second term is the product of the sequential allocation proposal probabilities from the launch state to the split state.

- The reverse merge proposal probability is calculated as  $q\{(\mathbf{Z}, \boldsymbol{\theta}) | (\mathbf{Z}^{\text{split}}, \boldsymbol{\theta}^{\text{split}}), \cdot\} = 1/J$ . This probability is determined by uniformly selecting one cluster from a set of  $J$  clusters for merging, while keeping the second cluster fixed as the  $(J + 1)$ -th cluster. The two clusters are then merged into the first cluster that was chosen.
- The merge proposal probability is calculated as  $q\{(\mathbf{Z}^{\text{merge}}, \boldsymbol{\theta}^{\text{merge}}) | (\mathbf{Z}, \boldsymbol{\theta}), \cdot\} = 1/\{J(J - 1)\}$ . The proposal uniformly selects two clusters from a set of  $J$  clusters, and merges the two clusters into the first cluster that was chosen.
- The reverse split proposal probability  $q\{(\mathbf{Z}, \boldsymbol{\theta}) | (\mathbf{Z}^{\text{merge}}, \boldsymbol{\theta}^{\text{merge}}), \cdot\}$  is calculated in the same way as the

split proposal probability. It is calculated by multiplying two terms in the last equation as

$$\begin{aligned} q\{(\mathbf{Z}, \boldsymbol{\theta}) | (\mathbf{Z}^{\text{merge}}, \boldsymbol{\theta}^{\text{merge}}), \cdot\} &= q\{\mathbf{Z} | \boldsymbol{\theta}, (\mathbf{Z}^{\text{merge}}, \boldsymbol{\theta}^{\text{merge}}), \cdot\} q\{\boldsymbol{\theta} | (\mathbf{Z}^{\text{merge}}, \boldsymbol{\theta}^{\text{merge}}), \cdot\} \\ &= q(\mathbf{Z} | \boldsymbol{\theta}, \mathbf{Z}^{\text{merge}}, \cdot) \\ &= \left(\frac{1}{2}\right)^{d_j} \prod_{m \in \mathcal{I}_{d_j}} p(Z_m^{\text{merge}} = z_m | \mathbf{Z}_{-m}^{\text{merge}}, \boldsymbol{\theta}, \cdot). \end{aligned}$$

The first term is the probability of proposing a split move from the merged state to a random launch state  $(1/2^{d_j})$ . The second term is the product of the sequential allocation proposal probabilities from the launch state to the original state.

- The ratio of likelihoods and prior distributions can be calculated by plugging in their forms provided in Sections 3.3 and 3.4. The ratio of covariance parameter prior distributions can be simplified as

$$\frac{p(\boldsymbol{\theta}^*)}{p(\boldsymbol{\theta})} = \frac{p(\rho_\ell^* | \cdot) p(\sigma_\ell^{2*} | \cdot)}{p(\rho_\ell | \cdot) p(\sigma_\ell^2 | \cdot)},$$

where  $\ell$  takes the value of either  $(J + 1)$  or  $j'$  depending on whether a split or merge proposal is selected, respectively.

## 5 Simulations

To evaluate the performance of the proposed clustering algorithm for grouping covariance sub-matrices, two sets of simulations with very large values of  $M$  and  $J$  are conducted. To mimic our real data example, we set  $N$  to be of the same order as  $M$ . In the first simulation, the true partition is generated from a Uniform distribution with equal cluster sizes. In the second simulation, the true partition is generated from a Dirichlet process prior. In both simulations,  $\mathbf{X}_i$  consists of  $p = 5$  covariates, including an intercept  $X_{i1}$ . The covariates  $X_{i2}$  and  $X_{i3}$  are generated from Binomial distributions with success probabilities of 0.5 and 0.7, respectively. The covariate  $X_{i4}$  is generated from a standard Gaussian distribution, and the last covariate  $X_{i5}$  is the interaction term between  $X_{i2}$  and  $X_{i4}$ .

We specify the maximum number of allowable clusters  $K$  to be  $M/2$ . The variance tuning parameter  $\lambda$  of Walker's slice sampler for the correlating parameters is set to 10. The prior specifications include setting  $\tau = 1$  for the regression coefficients  $\beta_q$ ,  $q = 1, \dots, p$  which results in a prior distribution of  $\mathcal{N}_M(\mathbf{0}, \mathbf{I}_M)$ . The variance parameters  $\sigma_j^2$  have prior distribution Inv-Gamma(2.01, 1.01). The transformed correlation parameters  $\eta_j$  have prior distribution Beta(2.01, 1.01). It is worth noting that the upper bound for the support of  $\rho_j$  is typically 1 for most covariance structures. To avoid computational issues arising from near-singular correlation sub-matrices, we set the upper bound for  $\rho_j$  to be 0.95. The Dirichlet process scale parameter  $\alpha$  is assigned the prior Gamma( $K + 0.01$ , 1.01). This choice ensures that the prior mean for  $\alpha$  is approximately equal to  $K$ , effectively setting the initial number of clusters as large as possible. As discussed in [Hastie et al. \(2015\)](#), it is recommended to set the initial number of clusters to be large in order to achieve convergence of the posterior distribution of  $\alpha$ . The simulation results are compared across 50 simulated data sets each run for 2000 iterations. For the HTSM sampler, we set the length of the first phase to half of the total number of iterations, specifically 1000.

In the first simulation, the performance of the model is evaluated assuming that the true partition is from

a Uniform distribution with equal cluster sizes,  $J = M/5$ , and three different settings are considered. The first setting considers dimensions  $M = 500$  and  $N = 500$  with a homogeneous compound symmetric (CS) covariance structure, where the same  $\rho$  and  $\sigma^2$  are assumed for all clusters. The true  $\rho$  and  $\sigma^2$  are set to 0.7 and 1.1, respectively. The second setting also considers dimensions  $M = 500$  and  $n = 500$ , but with a more complex heterogeneous generalized AR(1) covariance structure (Murray and Helms, 1990). Here, different sets of  $\rho_j$  and  $\sigma_j^2$  are assumed for each cluster. For each cluster, the true  $\rho_j$  is sampled from a uniform sequence with a spacing of 0.05 between 0.4 and 0.9, and the true  $\sigma_j^2$  is sampled from a uniform sequence with a spacing of 0.05 between 0.95 and 1.5. The generalized AR(1) covariance structure is defined by:

$$\text{Cov}\{y_i(\mathbf{s}_\ell), y_i(\mathbf{s}_k)\} = \sigma_j^2 \begin{cases} \rho_j^{\{d(s_\ell, s_k)\}^\nu} & \ell \neq k, \\ 1 & \ell = k. \end{cases}$$

Here,  $\mathbf{s}_m \in \mathbb{R}$ ,  $m = 1, \dots, M$  with  $d(s_\ell, s_k)$  the Euclidean distance between two locations. The decay speed parameter is set to  $\nu = 0.2$ . The third and most complicated setting considers dimensions  $M = 1000$  and  $N = 1000$ , and uses a heterogeneous Matérn covariance structure (Matérn, 1986) with shape parameter  $\nu = 1.5$ . Each  $\rho_j$  and  $\sigma_j^2$  is generated in the same manner as in the second setting. The Matérn covariance structure with  $\nu = 1.5$  is defined as follows:

$$\text{Cov}\{y_i(\mathbf{s}_\ell), y_i(\mathbf{s}_k)\} = \sigma_j^2 \begin{cases} \left\{1 + \frac{\sqrt{3}d(s_\ell, s_k)}{\rho_j}\right\} \exp\left\{-\frac{\sqrt{3}d(s_\ell, s_k)}{\rho_j}\right\} & \ell \neq k, \\ 1 & \ell = k. \end{cases}$$

Here,  $\mathbf{s}_m \in \mathbb{R}^2$ , with  $d(s_\ell, s_k)$  the Euclidean distance between two locations divided by 20.

Figure 3 displays the average posterior distribution of  $\mathbf{Z}$  across 50 simulations for the three settings. As the complexity of the covariance structure increases, the average number of partitions visited also increases, while the posterior probability of the MAP decreases. This suggests that a greater number of iterations is needed to identify the true partition as the complexity increases. In addition, the 95% percentile intervals of the posterior probability of the MAP derived from the 50 simulations become wider with increasing complexity, indicating that some simulations fail to accurately identify the correct partition. Among the 50 simulations of homogeneous CS, the true partition was identified as the MAP estimate in all cases, while the MAP estimate identifies the true partition in 49 out of 50 simulations of heterogeneous AR(1), and 46 out of 50 simulations of heterogeneous Matérn.

Table 1 presents the average coverage rates for a 95% credible interval across 50 simulations for  $\rho$ ,  $\sigma^2$ , and  $\mathbf{B}$ . The coverage rates are computed from the subset of iterations where  $\mathbf{Z}$  is equal to its MAP estimate. The table shows that the desired 95% level is achieved for all three settings, with slightly conservative inference. In the homogeneous CS setting, the dimensions of  $\rho$  and  $\sigma^2$  are both one, making it an easy problem for the model to identify the distribution of these two parameters. The posterior distributions for  $\rho$ ,  $\sigma^2$ , and  $\mathbf{B}$  are presented based on the MAP estimate of  $\mathbf{Z}$  because their posterior distributions depend on the value of  $\mathbf{Z}$ . When the estimate of  $\mathbf{Z}$  is close to the true partition, the conditional posterior distributions are likely centered around the true values. However, for estimates of  $\mathbf{Z}$  that are farther from the true partition, the posterior distributions are likely centered around other values, leading to multi-modal marginal posterior distributions.

In the second simulation, the true partition is assumed to be from a  $\text{DP}(6, P_0)$ , and two settings are

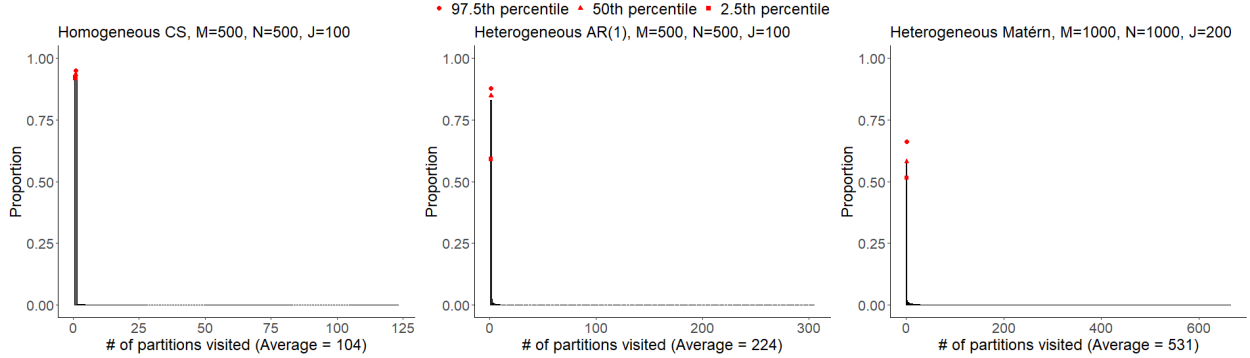


Figure 3: First simulation – Plot of posterior distribution of  $\mathbf{Z}$  averaged across 50 simulations, assuming a uniform true partition. The red points are the 95% percentile intervals of the probability of MAPs across the 50 simulations.

|                      | $M$  | $N$  | $J$ | coverage rate (sd) |             |              |
|----------------------|------|------|-----|--------------------|-------------|--------------|
|                      |      |      |     | $\rho$             | $\sigma^2$  | $\mathbf{B}$ |
| homogeneous CS       | 500  | 500  | 100 | 1.00 (0.00)        | 1.00 (0.00) | 0.95 (0.01)  |
| heterogeneous AR(1)  | 500  | 500  | 100 | 0.96 (0.07)        | 0.97 (0.05) | 0.95 (0.01)  |
| heterogeneous Matérn | 1000 | 1000 | 200 | 0.96 (0.14)        | 0.97 (0.08) | 0.95 (0.01)  |

Table 1: First simulation – Summary of coverage rates for a 95% credible interval, averaged across 50 simulations for  $\rho, \sigma^2, \mathbf{B}$ , assuming a uniform true partition. Standard deviations are in parentheses. The coverage rates are computed from the subset of iterations where  $\mathbf{Z}$  is equal to its MAP estimate.

considered. The first setting has dimensions  $M = 500, N = 500, J = 23$ , and a heterogeneous CS covariance structure. The second setting also has a heterogeneous CS covariance structure, but with larger dimensions  $M = 1000, N = 1000$ , and  $J = 37$ . The sets of  $\rho_j$  and  $\sigma_j^2$  are sampled in the same way as in the first simulation. Figure 4a shows the true partition for both settings, where the scale parameter  $\alpha$  is set to 6. This setting allows for a small number of very large clusters and a moderate number of size one clusters for the true partition.

The true partition was identified as the MAP estimate in all 50 simulations of heterogeneous CS with  $M = 500$  and of heterogeneous CS with  $M = 1000$ . Figure 4b shows that the average probability assigned to the MAP estimate is approximately 0.5 for both settings due to the proposed HTSM algorithm’s tail moves during the second phase of the MCMC. As the true partition has a moderate amount of size one clusters, the sampler mostly identifies the true partition during the second phase. Note that in the first simulation, the true partition was mostly identified during the first phase, leading to higher posterior probability of the MAPs than the second simulation. Table 2 shows that the desired 95% level is achieved for the average coverage rates of credible intervals across 50 simulations for  $\rho, \sigma^2$ , and  $\mathbf{B}$ .

It should be noted that the second simulation only assumes the CS covariance structure. When we consider covariance functions that rely on distances between measurements, estimating the true partition becomes challenging, particularly when dealing with large cluster sizes. In the case of a very large cluster, even with a slow decay rate, the off-diagonal terms of the covariance sub-matrix can be small, making it difficult to differentiate this covariance matrix from a combination of several moderately sized sub-matrices. It is important to highlight that this challenge primarily arises in high-dimensional settings where  $M$  is large.

Recalling the illustrative example in Figure 1, we were able to successfully identify the true partitions using a generalized AR(1) structure for a moderately sized problem ( $M = 100$  and  $N = 100$ ).

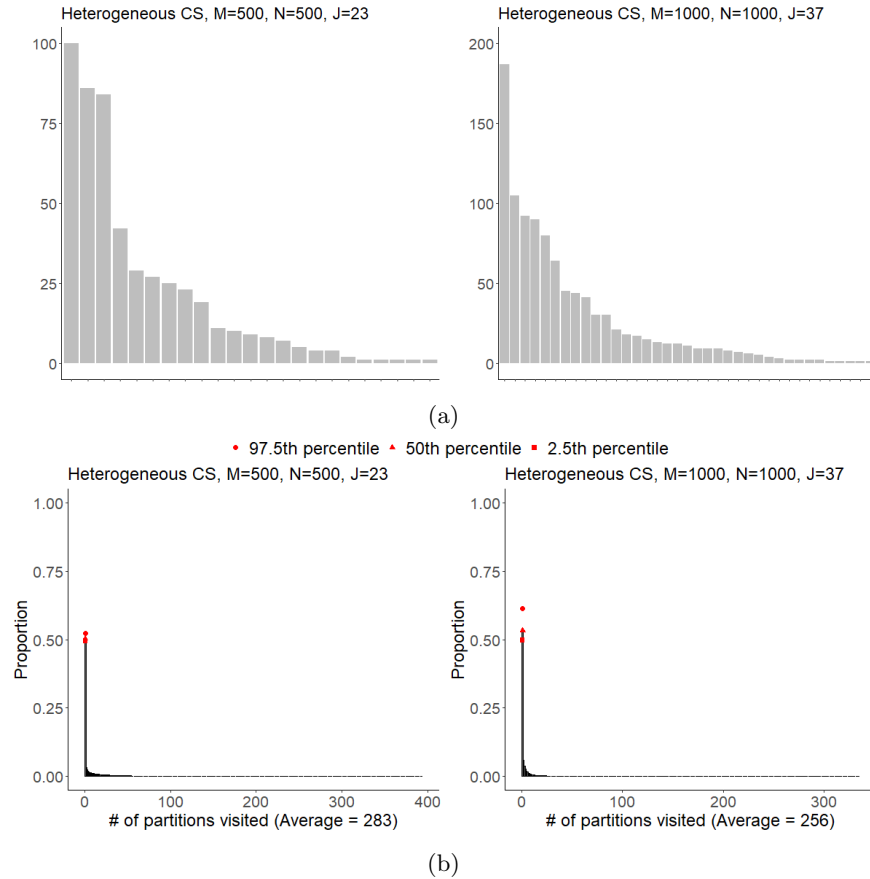


Figure 4: Second simulation – (a) Plot of the true partition generated from a  $DP(6, P_0)$ . The partition labels are sorted by block size from largest to smallest (top). (b) Plot of posterior distribution of  $\mathbf{Z}$  averaged across 50 simulations. The red points are the 95% percentile intervals of the probability of MAPs across the 50 simulations.

|                  | $M$  | $N$  | $J$ | coverage rate (SD) |             |              |
|------------------|------|------|-----|--------------------|-------------|--------------|
|                  |      |      |     | $\rho$             | $\sigma^2$  | $\mathbf{B}$ |
| heterogeneous CS | 500  | 500  | 23  | 0.99 (0.02)        | 0.97 (0.03) | 0.95 (0.02)  |
| heterogeneous CS | 1000 | 1000 | 37  | 0.99 (0.02)        | 0.97 (0.03) | 0.95 (0.01)  |

Table 2: Second simulation – Summary of coverage rates for a 95% credible interval, averaged across 50 simulations for  $\rho, \sigma^2, \mathbf{B}$ , assuming a  $DP(6, P_0)$  true partition. Standard deviations are in parentheses. The coverage rates are computed from the subset of iterations where  $\mathbf{Z}$  is equal to its MAP estimate.

## 6 Estimating brain co-activation regions

### 6.1 ABIDE data and problem descriptions

Numerous studies have investigated the complex relationship between ASD and attention-deficit/hyperactivity disorder (ADHD) as co-occurring disorders. However, there is still limited understanding of the functional network connectivity between specific brain regions associated with ASD and ADHD. In this section, we use our proposed Bayesian clustering approach for covariance structures to identify regions of co-activation in the Autism Brain Imaging Data Exchange (ABIDE) dataset (Di Martino et al., 2014). We consider rfMRI connectivity between  $M = 1000$  ROIs defined by the hierarchical multi-resolution parcellation introduced in Schaefer et al. (2018). From the various versions of the Schaefer parcellation, we specifically adopt the 17-network parcellation provided by Kong et al. (2021).

Our goal is to investigate both within-network and between-network functional connectivity by identifying clusters of correlated ROIs that display co-activation patterns in school-age, male children diagnosed with both ASD and ADHD. To achieve this, we compare two distinct groups of individuals selected from the same participating sites within the dataset. The first group consists of 21 school-age, male children diagnosed with both ASD and ADHD, referred to as the ASD-coADHD group. The second group comprises 52 school-age, male children diagnosed with ASD but without ADHD, referred to as the ASD-nonADHD group.

In each group, we denote the number of subjects as  $n$ . The length of the rfMRI time series with a lag of 2 for the  $\ell$ -th subject is represented by  $T_\ell$ . By incorporating a lag of 2, we ensure that the time points are sufficiently spaced apart and independent; see plots in the Supplementary Material. The total length of the concatenated rfMRI outcomes for all  $n$  individuals is defined as  $N = \sum_{\ell=1}^n T_\ell$ . Specifically, for the ASD-coADHD group,  $N = 1755$ , and for the ASD-nonADHD group,  $N = 4594$ . As the rfMRI outcome is an average across voxels within each ROI, the outcomes are approximately independently multivariate Gaussian due to the Central Limit Theorem. The covariates  $\mathbf{X}_i \in \mathbb{R}^n$ ,  $i = 1, \dots, N$ , correspond to  $\mathbf{e}_\ell \in \mathbb{R}^n$  for each  $\ell \in \{1, \dots, n\}$ . This representation gives a covariate corresponding to the indicator that the  $i$ -th outcome belongs to a time point for the  $\ell$ -th individual.

To account for noise in the rfMRI time series, we adopt a compound symmetric (CS) covariance structure that includes a nugget effect  $\xi$ . This structure implies that  $\mathbb{V}\{\mathbf{y}_{i,\text{perm}}(\mathcal{S})\} = \boldsymbol{\Sigma}_{\text{perm}}(\mathcal{S}; \boldsymbol{\theta}) + \xi \mathbf{I}_M$ , where the CS structure characterizes spatial variations in the covariance submatrices of  $\boldsymbol{\Sigma}_{\text{perm}}$ , and  $\xi$  captures variation from an independent error term. In our data analysis, we set  $\xi = 0.01$ . The selection of the CS structure is motivated by our interest in exploring functional connectivity between ROIs, which does not necessarily depend on spatial distance between the ROIs.

For both groups, we perform MCMC runs for 4000 iterations for each of 50 different seeds. The MCMC tuning parameters and prior specifications are set to be consistent with those in Section 5. The results obtained from the 50 different seeds are combined to obtain the maximum a posteriori (MAP) estimate of  $\mathbf{Z}$  and an estimate of the posterior mode for  $\boldsymbol{\rho}$  conditioned on the MAP estimate of  $\mathbf{Z}$ . These estimates are then used to generate the estimated correlation matrix, or connectivity matrix, presented below.

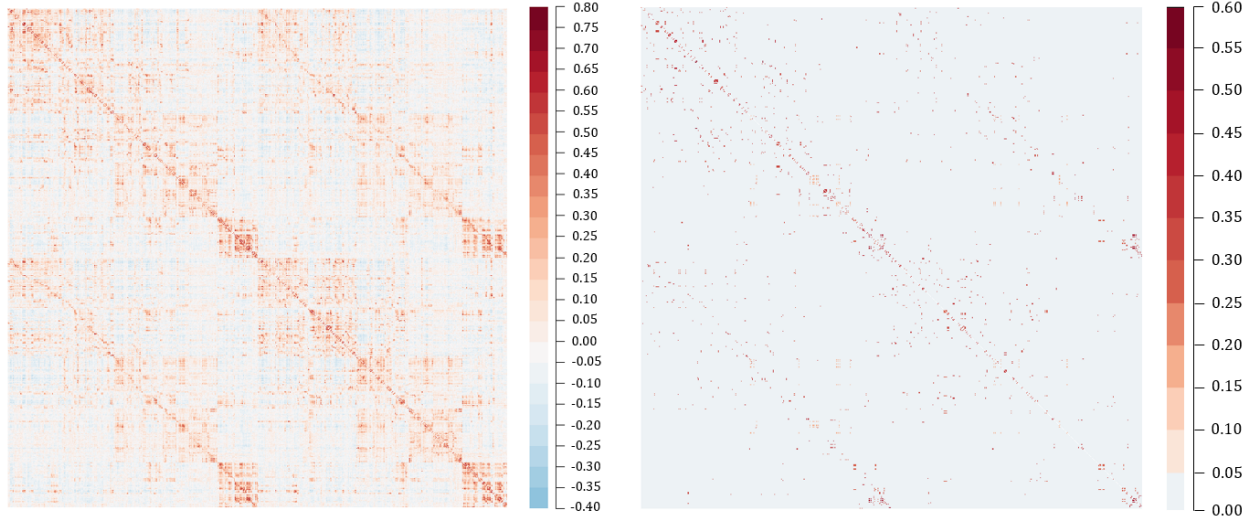


Figure 5: Connectivity matrix (left) and the estimated correlation matrix (right) for the ASD-coADHD group. The initial 500 ROIs correspond to the 17 networks of the left hemisphere, while the latter 500 ROIs correspond to the 17 networks of the right hemisphere.

## 6.2 Results from estimating functional connectivity

Figure 5 displays the sample connectivity matrix and the estimated correlation matrix for the ASD-coADHD group. We can visually identify co-activation patterns highlighted in red along both the diagonals and the off-diagonals, forming a banded structure. By the ordering of ROIs in the 17-network parcellation, the first 500 ROIs correspond to the 17 networks of the left hemisphere, while the last 500 ROIs correspond to the 17 networks of the right hemisphere. Consequently, we can interpret the co-activation patterns along the diagonals as indicative of functional connectivity within each hemisphere, and the co-activation patterns along the off-diagonals as indicative of functional connectivity between the two hemispheres. Visual examination of the estimated correlation matrix shows that our proposed approach effectively captures the banded structure of the co-activation patterns observed in the sample connectivity matrix. The plots for the ASD-nonADHD group are not presented here as they exhibit similar patterns to the ASD-coADHD group.

To identify the correlated (or co-activated) groups of ROIs, we calculate the posterior similarity matrix. This matrix comprises the empirically estimated posterior probabilities, obtained from the MCMC runs, that pairs of ROIs belong to the same cluster. Figure 6 presents the similarity matrix for the ASD-coADHD group; see the Supplementary Material for the similarity matrix of the ASD-nonADHD group. Notably, the banded structure observed in the sample connectivity matrix is also evident in the similarity matrix.

## 6.3 Interpreting functional connectivity within and between networks

To achieve the highest possible accuracy in identifying correlated groups of ROIs, we focus on pairwise similarities where the similarity value is equal to or greater than 90%. Our objective is to find groups of correlated ROIs that are unique to the ASD-coADHD group. To accomplish this, we exclude similarity pairs that are observed in both the ASD-coADHD group and the ASD-nonADHD group, as these pairs indicate common connections shared by both groups. Subsequently, from the remaining similarity pairs, we identify

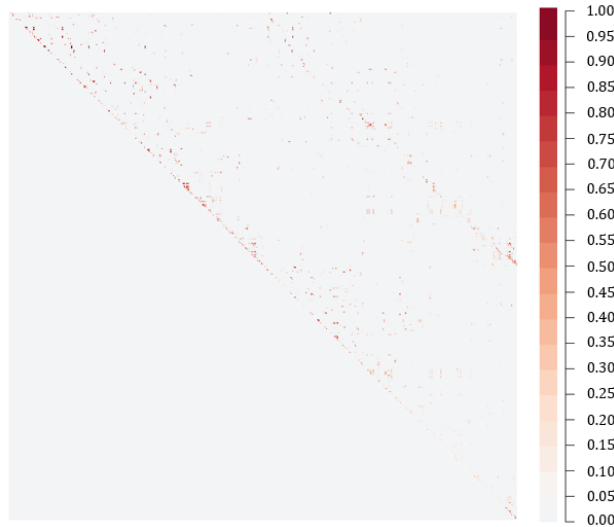


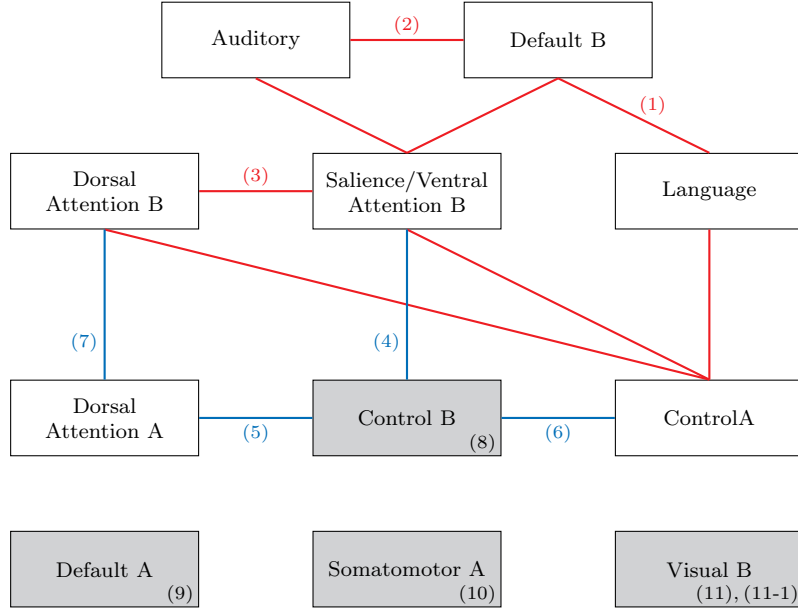
Figure 6: Posterior similarity matrix indicating the probability that pairs of ROIs belong to the same cluster for the ASD-coADHD group.

the correlated groups of ROIs containing at least three correlated ROIs within the group.

From the identified correlated groups of ROIs, we examine the functional connectivity within and between the 17 networks. The results of this analysis are summarized in Figure 7. In the figure, each brain region name is constructed by combining the hemisphere, network name, and component name. For instance, “LH-Default B-temporal” indicates that the brain region belongs to the left hemisphere (LH), within the Default B network, and corresponds to the temporal component. To validate our findings, we compare them with existing literature on network connectivity in ASD, ADHD, and ASD-coADHD groups. Notably, our approach has the advantage of identifying groups of interconnected networks, which sets it apart from many studies that primarily focus on pairwise relationships between networks. The following presents a brief evaluation of our findings in relation to those documented in the existing literature.

Previous research in ADHD, such as the comprehensive review by Castellanos and Aoki (2016), suggests the involvement of several networks, including the Default, Cognitive Control (Frontoparietal), and Attention (Dorsal, Ventral, Salience) networks, in ADHD. We also find similar relationships in our findings for between-network connectivity ((1)-(3) in Figure 7). Moreover, Blomberg et al. (2022) identified the interconnectivity between the Default, Salience/Ventral Attention, and Auditory networks in adults with ADHD, specifically in relation to auditory distraction.

We have identified specific network connections that align with existing literature in ASD. Gao et al. (2019) found increased connectivity between language regions and the posterior cingulate cortex, which belongs to networks Default A-C in our parcellation. This finding aligns with our observations of between-network connectivity involving the Language and Default B networks. Yerys et al. (2015) noted interactions between the Default Mode Network (DMN) and the Salience network, which is in line with our findings of between-network connectivity between the Default B and Salience/Ventral Attention B networks. Farrant and Uddin (2016) found hyper-connectivity within the dorsal and ventral attention networks in children with ASD, which supports our findings of pairwise connectivity between the Dorsal Attention A and Dorsal Attention B



**Between-network connectivity**

- (1) LH-Default B-temporal; LH-Saliency/Ventral Attention B-temporal; LH-Control A-temporal; LH-Language-temporal
- (2) LH-Default B-inferior parietal lobule; LH-Auditory-parietal occipital; LH-Saliency/Ventral Attention B-temporal
- (3) LH-Saliency/Ventral Attention B-inferior frontal gyrus; LH-Dorsal Attention B-precentral ventral; LH-Control A-lateral prefrontal cortex
- (4) LH-Control B-inferior parietal lobule; LH-Saliency/Ventral Attention B-inferior parietal lobule
- (5) LH-Control B-intraparietal sulcus; LH-Dorsal Attention A-intraparietal sulcus
- (6) LH-Control A-intraparietal sulcus; LH-Control B-intraparietal sulcus
- (7) LH-Dorsal Attention A-intraparietal sulcus; LH-Dorsal Attention B-post central; LH-Dorsal Attention B-superior parietal lobule

**Within-network connectivity**

- (8) LH-Control B-intraparietal sulcus
- (9) LH-Default A-medial prefrontal cortex; RH-Default A-medial prefrontal cortex
- (10) LH-Somatomotor A
- (11) LH-Visual B-striate cortex; RH-Visual B-striate cortex
- (11-1) LH-Visual B-striate cortex

Figure 7: Summary of functional connectivity within and between the 17 networks. The red lines represent connectivity between more than three networks. The blue lines represent connectivity between two networks. The highlighted grey colors indicate within-network connectivity. The brain region names are derived by combining the hemisphere, network name, and component name.

networks. Furthermore, [Jung et al. \(2019\)](#) identified increased somatomotor network connectivity in boys with ASD, which is consistent with our observations of within-network connectivity within the Somatomotor A network.

[Yerys et al. \(2019\)](#) found functional connectivity within and between the Frontoparietal and Saliency/Ventral Attention subnetworks for both ASD and ADHD groups, providing support for our findings of connectivity between the Control A and Control B networks. [Jung et al. \(2019\)](#) found increased visual network connectivity within boys with ADHD compared to boys with ASD, which aligns with our within-network connectivity in the Visual B network. [Wang et al. \(2021\)](#) showed increased between-network connectivity between the

Ventral Attention and Dorsal Attention networks, as well as between the Ventral Attention and Control networks for the ASD-coADHD group. This agrees with our observations of pairwise connectivity between the Salience/Ventral Attention B and Dorsal Attention B networks, as well as the pairwise connectivity between the Salience/Ventral Attention B and Control A networks.

In summary, our data analysis has revealed that a large number of the within-network and between-network connections we identified are consistent with findings reported in existing literature. Additionally, we have identified connections that have not been specifically studied in published literature, which highlights the insights provided by our analysis. Referring back to the previous paragraphs, we have found pairwise connections between the Language and Default B networks, and the Default B and Salience/Ventral Attention B networks, which have been reported in the literature on ASD regarding the between-network connectivity (1) in Figure 7. Moreover, we have also observed pairwise network connectivity involving the Language and Salience/Ventral Attention B networks, and between-network connectivity among the three networks: Default B, Salience/Ventral Attention B, and Language, which have not been previously identified in the literature. These findings demonstrate the potential of our method as an effective tool for studying network connectivities. The concurrence between our findings and the literature suggests that the brain network connections we have identified are relevant to all three groups: ASD, ADHD, and ASD-coADHD.

## 7 Conclusions

In this study, we have introduced a Bayesian clustering approach that effectively groups covariance submatrices associated with high-dimensional Gaussian outcomes. Our method incorporates the stick-breaking construction of the Dirichlet process prior, enabling the identification of independent subgroups of outcomes. We proposed a new sampler, the Head-Tail Split-Merge algorithm, to improve the mixing of the MCMC. Through extensive simulations, we have validated the applicability of our approach in settings involving large dimensions of  $M$  and  $J$ . Additionally, we have successfully applied our method to investigate co-activation patterns in ASD and ADHD, where we have discovered both between-network and within-network functional connectivity patterns in the brain that align with findings in the existing literature.

In future research, it would be worthwhile to explore more comprehensive covariance structures to model functional connectivity in the brain for individuals with ASD. Possible directions include incorporating covariate effects into the covariance structure or considering ways to incorporate negative correlations in the covariance matrix. As observed in Figure 5, the connectivity matrix exhibits not only co-activation patterns (positive correlation) but also reciprocal activation patterns (negative correlation). While the compound symmetry structure allows for negative correlations, its lower bound  $-1/(M-1)$  tends to zero as  $M$  increases, making it insufficient to capture reciprocal activation patterns. Further research in this area could explore separate modeling of both types of patterns.

## Acknowledgements

The authors are grateful to the participants of the ABIDE study, and the ABIDE study organizers and members who aggregated, preprocessed and shared the ABIDE data.

## References

- Sudipto Banerjee, Alan E. Gelfand, Andrew O. Finley, and Huiyan Sang. Gaussian predictive process models for large spatial data sets. *Journal of the Royal Statistical Society: Series B (Statistical Methodology)*, 70(5):825–848, 2008. doi: 10.1111/j.1467-9868.2008.00663.x. URL <https://doi.org/10.1111/j.1467-9868.2008.00663.x>.
- Joanne C Beer, Howard J Aizenstein, Stewart J Anderson, and Robert T Krafty. Incorporating prior information with fused sparse group lasso: Application to prediction of clinical measures from neuroimages. *Biometrics*, 75(4):1299–1309, 12 2019. doi: 10.1111/biom.13075. URL <https://doi.org/10.1111/biom.13075>.
- David M. Blei and Michael I. Jordan. Variational inference for Dirichlet process mixtures. *Bayesian Analysis*, 1(1):121 – 143, 2006. doi: 10.1214/06-BA104. URL <https://doi.org/10.1214/06-BA104>.
- Rina Blomberg, Carine Signoret, Henrik Danielsson, Irene Perini, Jerker Rönnerberg, and Andrea Johansson Capusan. Aberrant resting-state connectivity of auditory, ventral attention/salience and default-mode networks in adults with attention deficit hyperactivity disorder. *Frontiers in Neuroscience*, 16, 2022. ISSN 1662-453X. doi: 10.3389/fnins.2022.972730. URL <https://www.frontiersin.org/articles/10.3389/fnins.2022.972730>.
- Alexandre Bouchard-Côté, Arnaud Doucet, and Andrew Roth. Particle gibbs split-merge sampling for bayesian inference in mixture models. *J. Mach. Learn. Res.*, 18(1):868–906, jan 2017. ISSN 1532-4435.
- F. Xavier Castellanos and Yuta Aoki. Intrinsic functional connectivity in attention-deficit/hyperactivity disorder: A science in development. *Biological Psychiatry Cognitive Neuroscience and Neuroimaging*, 1: 253–261, 2016. ISSN 2451-9022. doi: 10.1016/j.bpsc.2016.03.004.
- Jason Chang and John W Fisher III. Parallel sampling of dp mixture models using sub-cluster splits. In C.J. Burges, L. Bottou, M. Welling, Z. Ghahramani, and K.Q. Weinberger, editors, *Advances in Neural Information Processing Systems*, volume 26. Curran Associates, Inc., 2013. URL [https://proceedings.neurips.cc/paper\\_files/paper/2013/file/bca82e41ee7b0833588399b1fcd177c7-Paper.pdf](https://proceedings.neurips.cc/paper_files/paper/2013/file/bca82e41ee7b0833588399b1fcd177c7-Paper.pdf).
- David B Dahl. An improved merge-split sampler for conjugate dirichlet process mixture models. Technical report, University of Wisconsin - Madison, 2003.
- Sameer K. Deshpande, Veronika Ročková, and Edward I. George. Simultaneous variable and covariance selection with the multivariate spike-and-slab lasso. *Journal of Computational and Graphical Statistics*, 28(4):921–931, 2019. doi: 10.1080/10618600.2019.1593179. URL <https://doi.org/10.1080/10618600.2019.1593179>.
- Adriana Di Martino, Chao-Gan Yan, Qixiang Li, and et al. The autism brain imaging data exchange: towards a large-scale evaluation of the intrinsic brain architecture in autism. *Molecular Psychiatry*, 19(6):659–667, 2014. doi: 10.1038/mp.2013.78. URL <https://doi.org/10.1038/mp.2013.78>.
- Kristafor Farrant and Lucina Q Uddin. Atypical development of dorsal and ventral attention networks in autism. *Developmental Science*, 19:550–563, 2016. ISSN 1363-755X. doi: 10.1111/desc.12359.

- Thomas S. Ferguson. A Bayesian Analysis of Some Nonparametric Problems. *The Annals of Statistics*, 1(2): 209 – 230, 1973. doi: 10.1214/aos/1176342360. URL <https://doi.org/10.1214/aos/1176342360>.
- Montserrat Fuentes. Approximate likelihood for large irregularly spaced spatial data. *Journal of the American Statistical Association*, 102(477):321–331, Mar 2007. doi: 10.1198/016214506000000852.
- Yangfeifei Gao, Annika Linke, Ruth Joanne Jao Keehn, Sanjana Punyamurthula, Afroz Jahedi, Kathleen Gates, Inna Fishman, and Ralph-Axel Müller. The language network in autism: Atypical functional connectivity with default mode and visual regions. *Autism Research*, 12(9):1344–1355, 2019. ISSN 1939-3792. doi: 10.1002/aur.2171. URL <https://doi.org/10.1002/aur.2171>.
- Sina Ghiassian, Russell Greiner, Ping Jin, and Matthew R G Brown. Using functional or structural magnetic resonance images and personal characteristic data to identify adhd and autism. *PLoS One*, 11(12):e0166934, 2016. ISSN 1932-6203. doi: 10.1371/journal.pone.0166934.
- Peter J. Green and Sylvia Richardson. Modelling heterogeneity with and without the dirichlet process. *Scandinavian Journal of Statistics*, 28(2):355–375, 2001. ISSN 03036898, 14679469. URL <http://www.jstor.org/stable/4616664>.
- Sungji Ha, In-Jung Sohn, Namwook Kim, Hyeon Jeong Sim, and Keun-Ah Cheon. Characteristics of brains in autism spectrum disorder: Structure, function and connectivity across the lifespan. *Experimental Neurobiology*, 24(4):273–284, 2015. doi: 10.5607/en.2015.24.4.273.
- David I. Hastie, Silvia Liverani, and Sylvia Richardson. Sampling from dirichlet process mixture models with unknown concentration parameter: mixing issues in large data implementations. *Statistics and Computing*, 25(5):1023–1037, 2015. URL <https://doi.org/10.1007/s11222-014-9471-3>.
- Jocelyn V Hull, Lisa B Dokovna, Zachary J Jacokes, Carinna M Torgerson, Andrei Irimia, and John Darrell Van Horn. Resting-state functional connectivity in autism spectrum disorders: A review. *Frontiers in psychiatry*, 7:205, 2016. doi: 10.3389/fpsy.2016.00205.
- Hemant Ishwaran and Lancelot F. James. Gibbs sampling methods for stick-breaking priors. *Journal of the American Statistical Association*, 96(453):161–173, 2001. ISSN 01621459. URL <http://www.jstor.org/stable/2670356>.
- Sonia Jain and Radford M. Neal. A split-merge markov chain monte carlo procedure for the dirichlet process mixture model. *Journal of Computational and Graphical Statistics*, 13(1):158–182, 2004. ISSN 10618600. URL <http://www.jstor.org/stable/1391150>.
- Minyoung Jung, Yiheng Tu, Joel Park, Kristen Jorgenson, Courtney Lang, Wenwen Song, and Jian Kong. Surface-based shared and distinct resting functional connectivity in attention-deficit hyperactivity disorder and autism spectrum disorder. *The British Journal of Psychiatry*, 214:339–344, 2019. ISSN 1472-1465. doi: 10.1192/bjp.2018.248.
- Cari G. Kaufman, Mark J. Schervish, and Douglas W. Nychka. Covariance tapering for likelihood-based estimation in large spatial data sets. *Journal of the American Statistical Association*, 103(484):1545–1555, 2008. doi: 10.1198/016214508000000959.

- Zakaria S. Khondker, Hongtu Zhu, Haitao Chu, Wei Lin, and Joseph G. Ibrahim. The bayesian covariance lasso. *Statistical Interface*, 6(2):243–259, Apr 2013. doi: 10.4310/sii.2013.v6.n2.a8.
- Ru Kong, Qing Yang, Evan Gordon, Aihuiping Xue, Xiaoxuan Yan, Csaba Orban, Xi-Nian Zuo, Nathan Spreng, Tian Ge, Avram Holmes, Simon Eickhoff, and B T Thomas Yeo. Individual-Specific Areal-Level Parcellations Improve Functional Connectivity Prediction of Behavior. *Cerebral Cortex*, 31(10):4477–4500, 05 2021. ISSN 1047-3211. doi: 10.1093/cercor/bhab101. URL <https://doi.org/10.1093/cercor/bhab101>.
- Y. Li, B. Nan, and J. Zhu. Multivariate sparse group lasso for the multivariate multiple linear regression with an arbitrary group structure. *Biometrics*, 71(2):354–363, Jun 2015. doi: 10.1111/biom.12292. Epub 2015 Mar 2.
- Yanxin Li and Stephen G. Walker. A latent slice sampling algorithm, 2020. URL <https://arxiv.org/abs/2010.08509>.
- Shan Luo and Zehua Chen. Feature selection by canonical correlation search in high-dimensional multiresponse models with complex group structures. *Journal of the American Statistical Association*, 115(531):1227–1235, 2020. doi: 10.1080/01621459.2019.1609972.
- Charles J Lynch, Lucina Q Uddin, Kaustubh Supekar, Amirah Khouzam, Jennifer Phillips, and Vinod Menon. Default mode network in childhood autism: posteromedial cortex heterogeneity and relationship with social deficits. *Biological psychiatry*, 74(3):212–219, 2013. doi: 10.1016/j.biopsych.2012.12.013.
- Bertil Matérn. *Spatial Variation*. Lecture Notes in Statistics. Springer New York, NY, 2 edition, 1986. doi: 10.1007/978-1-4615-7892-5. Originally published by the Swedish National Institute for Forestry Research, 1960.
- Antonietta Mira and Luke Tierney. Efficiency and convergence properties of slice samplers. *Scandinavian Journal of Statistics*, 29(1):1–12, 2002. ISSN 03036898, 14679469. URL <http://www.jstor.org/stable/4616695>.
- A. Mohammadi and E. C. Wit. Bayesian Structure Learning in Sparse Gaussian Graphical Models. *Bayesian Analysis*, 10(1):109 – 138, 2015. doi: 10.1214/14-BA889. URL <https://doi.org/10.1214/14-BA889>.
- Sharon C. Murray and Ronald W. Helms. Linear models with generalized ar(1) covariance structure for irregularly-timed data. 1990. URL <http://www.lib.ncsu.edu/resolver/1840.4/3988>.
- Radford M. Neal. Slice sampling. *The Annals of Statistics*, 31(3):705 – 767, 2003. doi: 10.1214/aos/1056562461. URL <https://doi.org/10.1214/aos/1056562461>.
- Douglas Nychka, Soutir Bandyopadhyay, Dorit Hammerling, Finn Lindgren, and Stephan Sain. A multiresolution gaussian process model for the analysis of large spatial datasets. *Journal of Computational and Graphical Statistics*, 24(2):579–599, 2015. doi: 10.1080/10618600.2014.914946.
- Omiros Papaspiliopoulos and Gareth O. Roberts. Retrospective markov chain monte carlo methods for dirichlet process hierarchical models. *Biometrika*, 95(1):169–186, 2008. ISSN 00063444, 14643510. URL <http://www.jstor.org/stable/20441450>.

- Gareth O. Roberts and Jeffrey S. Rosenthal. Convergence of slice sampler markov chains. *Journal of the Royal Statistical Society. Series B (Statistical Methodology)*, 61(3):643–660, 1999. ISSN 13697412, 14679868. URL <http://www.jstor.org/stable/2680728>.
- Alberto Roverato. Hyper inverse wishart distribution for non-decomposable graphs and its application to bayesian inference for gaussian graphical models. *Scandinavian Journal of Statistics*, 29(3):391–411, 2002. ISSN 03036898, 14679469. URL <http://www.jstor.org/stable/4616723>.
- S. Samanta, K. Khare, and G. Michailidis. A generalized likelihood-based bayesian approach for scalable joint regression and covariance selection in high dimensions. *Statistical Computing*, 32(47), 2022. doi: 10.1007/s11222-022-10102-5. URL <https://doi.org/10.1007/s11222-022-10102-5>.
- Alexander Schaefer, Ru Kong, Evan M. Gordon, Timothy O. Laumann, Xi-Nian Zuo, Avram J. Holmes, Simon B. Eickhoff, and B. T. Thomas Yeo. Local-global parcellation of the human cerebral cortex from intrinsic functional connectivity mri. *Cerebral Cortex*, 28(9):3095–3114, 2018. doi: 10.1093/cercor/bhx179.
- Jayaram Sethuraman. A constructive definition of dirichlet priors. *Statistica Sinica*, 4(2):639–650, 1994. ISSN 10170405, 19968507. URL <http://www.jstor.org/stable/24305538>.
- Michael L. Stein. Statistical properties of covariance tapers. *Journal of Computational and Graphical Statistics*, 22(4):866–885, 2013. doi: 10.1080/10618600.2012.719844.
- Stephen G. Walker. Sampling unnormalized probabilities: An alternative to the metropolis-hastings algorithm. *SIAM Journal on Scientific Computing*, 36(2):A482–A494, 2014. doi: 10.1137/130922549. URL <https://doi.org/10.1137/130922549>.
- Hao Wang. Bayesian Graphical Lasso Models and Efficient Posterior Computation. *Bayesian Analysis*, 7(4): 867 – 886, 2012. doi: 10.1214/12-BA729. URL <https://doi.org/10.1214/12-BA729>.
- Kai Wang, Ke Li, and Xiaoyu Niu. Altered functional connectivity in a triple-network model in autism with co-occurring attention deficit hyperactivity disorder. *Frontiers in Psychiatry*, 12:736755, 2021. ISSN 1664-0640. doi: 10.3389/fpsy.2021.736755.
- Wei Wang and Stuart J. Russell. A smart-dumb/dumb-smart algorithm for efficient split-merge mcmc. In *Conference on Uncertainty in Artificial Intelligence*, 2015.
- Sinead Williamson, Avinava Dubey, and Eric Xing. Parallel markov chain monte carlo for nonparametric mixture models. In *Proceedings of the 30th International Conference on Machine Learning*, volume 28, pages 98–106. PMLR, 2013.
- Benjamin E Yerys, Evan M Gordon, Danielle N Abrams, Theodore D Satterthwaite, Rachel Weinblatt, Kathryn F Jankowski, John Strang, Lauren Kenworthy, William D Gaillard, and Chandan J Vaidya. Default mode network segregation and social deficits in autism spectrum disorder: Evidence from non-medicated children. *NeuroImage. Clinical*, 9:223–32, 2015. ISSN 2213-1582. doi: 10.1016/j.nicl.2015.07.018. URL <https://www.ncbi.nlm.nih.gov/pmc/articles/PMC4573091/>.

Benjamin E Yerys, Birkan Tunç, Theodore D Satterthwaite, Ligia Antezana, Maya G Mosner, Jennifer R Bertollo, Lisa Guy, Robert T Schultz, and John D Herrington. Functional connectivity of frontoparietal and salience/ventral attention networks have independent associations with co-occurring attention-deficit/hyperactivity disorder symptoms in children with autism. *Biological Psychiatry: Cognitive Neuroscience and Neuroimaging*, 4(4):343–351, Apr 2019. ISSN 2451-9022. doi: 10.1016/j.bpsc.2018.12.012. URL <https://doi.org/10.1016/j.bpsc.2018.12.012>.